The effect of the nature of supports on the selective reduction of CO2 to CO catalysed by a supported single-site heterobimetallic iron–potassium complex

Abdulrahman Adamu Isah, Yahaya Nasiru, Fadila Hamachi, Jie Pan, Kai Szeto, Pierre-Yves Dugas, Cyril Godard, Aimery De mallmann, Mostafa Taoufik

The effect of the Nature of Supports on the Selective Reduction of CO_2 to CO Catalysed by Supported Single-Site Heterobimetallic Iron-Potassium Complex

Abdulrahman Adamu Isah,[a,c] Yahaya Nasiru,[a] Fadila Hamachi,[a] Jie Pan,[b] Kai C. Szeto,[a,] Pierre-Yves Dugas,[a] Cyril Godard,[b,*] Aimery De Mallmann,[a,] and Mostafa Taoufik[a,*]

[a]Université Lyon 1, Institut de Chimie Lyon, CPE Lyon CNRS, UMR 5128, CP2M, CPM, 43 Bd du 11 Novembre 1918, 69616 Villeurbanne Cedex, France.

[b]Departament de Química Física i Inorgànica, Universitat Rovira i Virgili, Tarragona 43007, Spain

[c]Department of Pure and Environmental Chemistry, Usmanu Danfodiyo University, Sokoto 840004, Nigeria

E-mail addresses: mostafa.taoufik@univ-lyon1.fr. ; cyril.godard@urv.cat,

ABSTRACT

The utilization of CO_2 for the production of value-added chemicals has attracted significant interest. Among various strategies, the selective catalytic hydrogenation to liquid hydrocarbons via a two-step process, first the reduction of CO_2 to CO through the reverse water–gas shift (RWGS) reaction, followed by CO conversion, is particularly promising. In this work, $[\{(THF)_2KFe(OtBu)_3\}_2]$ molecular complex was supported on various oxides in order to systematically investigate the influence of the support's physicochemical properties (neutral, basic, acidic, and redox) on the catalytic performance in RWGS reaction. A series of catalysts with 1 wt% Fe were synthesized and characterized by DRIFT, XRD, BET, HRTEM, EDX, ICP, EPR, and XAFS (specifically for ZrO_2-supported systems). Remarkably, catalysts supported on neutral (SiO_2, Al_2O_3) and basic (ZrO_2, MgO-Al_2O_3) oxides maintained close Fe–K proximity, exhibiting high catalytic activity and full selectivity toward CO (100%) in the RWGS reaction. Among these, the **FeK/ZrO_2-250** appears to be stable after 40 h on stream, which is supported by XAFS and TEM analyses. K^+ served as an electronic promoter as well as a structural stabilizer of the active Fe site, preventing agglomeration. In contrast, use of acidic or redox-active supports resulted in loss of the activity or the selectivity in CO during RWGS. The formation of methane is attributed to the dissociation of FeK species into Fe nanoparticles and the incorporation of K into the CeO_2 lattice or by exchange with acid sites of ZSM-5, Nb_2O_5 or SiO_2-Al_2O_3, thereby disrupting the critical Fe–K synergy. These findings underscore the pivotal role of support selection in preserving the structural and electronic integrity of Fe–K active sites. Supports that inhibit sintering and maintain the FeK single-site configuration are essential for achieving high activity, full CO selectivity, and long-term stability in the RWGS reaction.

Keywords: CO_2 hydrogenation; Reverse water gas shift; Iron–potassium catalyst; Surface organometallic chemistry; Catalyst support effects; Redox support; Acid–base properties; CO selectivity; Single-site catalyst; metal-support interaction.

1. Introduction

Recently, the catalytic reduction of CO_2 to CO via the Reverse Water Gas Shift (RWGS) reaction has gained attention from industries and academia due to the raising importance in the CO_2 conversion technology and the interest of using CO as a feedstock in the Fischer-Tropsch process, a mature technology for converting this intermediate into valuable chemicals and fuels.[1–7] However, due to high thermodynamic stability of CO_2, RWGS reaction is an endothermic process ($\Delta H° = 42.1$ kJ/mol) that requires higher temperatures and high H_2/CO_2 ratios to be optimal.[8–11] Although pressure does not influence its equilibrium, the reaction faces competition from undesired methanation and the exothermic Sabatier reaction, which are favored at lower temperatures and pressures (**Equations 1-3**).[12–15] At temperatures below 600°C, methane formation dominates, whereas higher temperatures (>600°C) enhance CO selectivity.[11,16] In order to reduce energy and capital costs, the reaction temperature should be kept as low as possible and simultaneously optimize the CO production with minimum CH_4 as undesired byproduct. Therefore, understanding the mechanisms, the structure of the active species and kinetics of the RWGS reaction is crucial for the catalyst design for syngas production. These strategies include varying the support, tuning metal-support interactions, adding reducible transition metal oxide promoters, forming bimetallic alloys, adding alkali metals, and enveloping metal particles.[17–20] Selecting an appropriate support is important to tune the activity and selectivity of this reaction. Various oxides such as SiO_2, ZrO_2, TiO_2, mullite (aluminum-silicate), Al_2O_3 and CeO_2 were reported as catalyst supports in RWGS reaction.[11,16,21,22] The authors described that redox and acid-base properties of the supports can greatly influence CO_2 adsorption/activation and the nature of the reaction intermediates and the mechanisms (redox and associative). SiO_2 and Al_2O_3 are neutral and irreducible supports,[17] and many studies indicated that these supports indirectly participate in the RWGS reaction by enhancing metal dispersion and CO_2 adsorption. For example, when Pt single site catalysts were supported on silica, it was proposed that CO_2 adsorbs at the interface between Pt and SiO_2 via hydrogen bonding between silanol groups.[16] This CO_2 adsorption strength enhances by 0.21 eV compared to unsupported Pt nanoparticle, thus allowing to the formation of formate species, intermediate for CO production.[16] Similarly,

the use of Al_2O_3 as an irreducible and amphoteric oxide for the dispersion of Pd single site catalysts provided high selectivity to CO compared to Pd supported on inert multiwall carbon nanotubes (MWCNT).[23] In order to explain this effect of the support, Bobadilla *et al*.[24] proposed that CO_2 reacts with the basic hydroxyl groups of Al_2O_3 to form bicarbonate species which, via hydrogen spillover from Pd, lead to the formation of aluminum formate intermediates that further decompose into CO.

$$CO_2 + H_2 \rightleftarrows CO + H_2O_{(g)} \qquad \Delta H^{o} = +41.3 \text{ kJ/mol} \qquad (1)$$

$$CO_2 + 4\,H_2 \rightleftarrows CH_4 + 2\,H_2O_{(g)} \qquad \Delta H^{o} = -164.7 \text{ kJ/mol} \qquad (2)$$

$$CO + 3H_2 \rightleftarrows CH_4 + H_2O_{(g)} \qquad \Delta H^{o} = -206.2 \text{ kJ/mol} \qquad (3)$$

Equations 1-3. RWGS, methanation and Sabatier reaction during CO_2 hydrogenation

The effect of an acidic support such as a zeolite (H-ZSM-5) was also reported for the conversion of CO_2 to CO.[25–27] For example, Wang *et al.*[27] compared CO_2 hydrogenation on Rh supported on zeolite such as H-ZSM-5 and pure silica MFI, revealing that neutral silica MFI modified by rhodium exhibited high CO selectivity with high CO_2 conversions. However, Rh supported on acidic support H-ZSM-5 showed moderate selectivity to CO with the formation of methane under the same conditions. Strong correlations were observed between the nanoporous environment and catalytic selectivity, indicating that neutral silica MFI minimized hydrogen spill over and favors the fast desorption of CO to limit total hydrogenation to methane.[27] Furthermore, the use of basic support such as zirconia was reported and revealed that the selectivity to CO depends on the nature of the metal and the metal loading.[28–30] Based on literature studies, the nature and properties of the supports thus have a strong effect on the catalyst activity and selectivity in the conversion of CO_2 to CO.

Redox supports such as TiO_2, CeO_2-ZrO_2 and CeO_2 are known to generate oxygen vacancies, particularly in the presence of an immobilized metal during the activation of H_2 and CO_2.[31] In the case of ceria-based catalysts, the catalytic performances in CO_2 hydrogenation were generally attributed to oxygen storage capacity, redox properties, and the ability to enhance reaction rates and selectivity.[32] CeO_2 is reported to possess unique synergistic effects when doped with other metal that improve their catalytic activity.[33] Using DFT calculation, Ceria supported copper and iron catalysts[34,35] were both reported and showed moderate activity for RWGS.[36] However, Ceria supported Ni and Co favored CO_2 methanation.[37] From these studies, the high activity of metal doped CeO_2 was attributed to the increase of the reducibility and consequently the number of oxygen vacancy.[38] However, the selectivity in

CO is favored when the dopants are well dispersed on ceria surface. On the other hand, the presence of metal nanoparticles on ceria surface increase the formation of undesired products such as methane.[39,40] Recently, the inherent relationships between the performance of transition metal (Fe, Co, Ni and Cu) doped CeO_2 catalysts, the concentration of transition metals doped onto CeO_2 surfaces, CO_2 binding strength, and the oxygen vacancy formation energy were explored for the RWGS. At low loading, Fe/CeO_2 showed low conversion (10 %) and high selectivity in CO (100 %) but at high temperature (600 °C). However, at temperatures lower than 500 °C, no activity in RWGS was reported due to the lack of synergistic effect between iron and Ceria at temperatures below 500 °C.[39] In addition to the effect of support, the presence of alkali metal ions was reported to enhance metal-support interactions for transition metal-based catalysts, leading to increased stability and thereby increased activity and CO selectivity.[36,41,42] The incorporation of potassium into Fe/Al_2O_3 with K/Fe of 1 resulted in a significant increase in CO formation rates compared to unpromoted Fe/Al_2O_3.[43] The increased basicity using K improves the adsorption of CO_2 by forming Lewis acid−base pairs that enhances CO_2 binding by chemisorption on the surface through electron transfer.[36] Thus, the potassium promoter activates a secondary pathway for CO formation, which may be the so-called associative pathway.[43] Based on this finding, we recently reported a well-defined supported single-site Fe RWGS catalyst with low Fe loading that essentially provided 100% selectivity to CO at 400 °C. The heterobimetallic FeK complex, $[\{(THF)_2KFe(O\textit{t}Bu)_3\}]_2$, containing K as metal cation, was grafted by Surface Organometallic Chemistry (SOMC) [44] onto partially dehydroxylated Al_2O_3 at 500 °C and characterized by ICP, IR, XPS, EDX, XAFS, and EPR. XAFS spectroscopy. The material consisted of an isolated anionic Fe(II) site coordinated by two tert-butoxide ligands and one anionic surface oxygen, associated with K^+. The postulated mechanism (**Scheme 1**)proceeds through H_2 activation to form an iron hydride, which evolves to an iron hydroxycarbonyl intermediate upon insertion of CO_2 that by further decomposition leads to CO.[45] Importantly, the Na and Li counterparts did not lead to substantial activity in RWGS.[45] Taking into account that the potassium in proximity of Fe has a significant effect on the activity and selectivity during the adsorption and the activation of CO_2, the modification of the nature and the properties (acidity, basicity and redox) of the supports may also affect the activity and the selectivity during CO_2 conversion to CO.

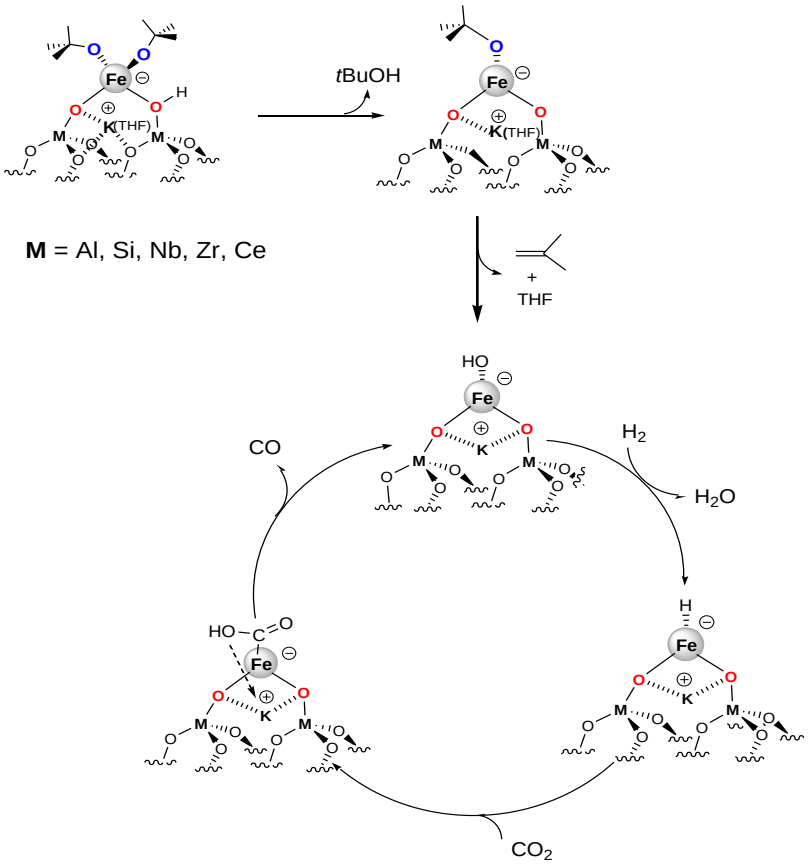

Scheme 1. Proposed mechanism for selective conversion of CO_2 to CO on supported anionic heterobimetallic Fe and K complex independent of the support (neutral, basic, acidic or redox).

Here, this approach was extended to study the effect of the nature of the supports (neutral, basic, acidic and redox) on activity and selectivity in RWGS. This methodology allowed us to study the combination of the two parameters (K and support properties) on the activity and selectivity to CO as well as for the validation of the proposed mechanism on supported anionic iron single active species. To ensure the aforementioned criteria, neutral (SiO_2), basic (MgO-Al_2O_3 (Pural) and ZrO_2), acidic (Nb_2O_5, SiO_2-Al_2O_3 and µ-H-ZSM-5) and redox (TiO_2, CeO_2 and $CeZrO_x$) supports were selected for the stabilization of the isolated iron species. The resulting materials were characterized using ICP, DRIFT, HRTEM, BET, EDX, EPR, XRD and XAFS for the catalyst based on Zirconia before and after catalysis. The catalysts were then tested for the reduction of CO_2 to CO.

2. Experimental methods

2.1 Chemicals and materials

All experiments were carried out under a controlled atmosphere, using Schlenk and glovebox techniques for organometallic synthesis. For the synthesis and treatment of supported

species, reactions were carried out using high-vacuum lines (*ca.* 1 mPa pressure) and gloveboxes. Pentane and THF were distilled from NaK and degassed using freeze-pump-thaw cycles. $FeBr_2$ and *t*BuOK were purchased from Aldrich and used as received.

2.2 Characterization of materials

All characterization was performed under an inert atmosphere, except for EDX/STEM/HRTEM for which sample preparation was carried out in air. Catalytic tests were performed in a ½'' stainless-steel continuous flow reactor connected to an online GC (Agilent Technologies 7890A) equipped with a FID (Jetanyzer^{TM}). The products were separated on a 30-m PLOT Q and CarbonPlot columns connected in series. Elemental analysis was carried out at the Mikroanalytiches Labor Pascher, Ramgen, Germany, and CREALINS, Villeurbanne, France, using an iCAP 6500 Duo inductively-coupled plasma atomic emission spectrometer (Thermo Scientific). All samples sent for elemental analysis were prepared under Ar and sealed under high vacuum (10^{-5} mbar).

Infrared spectra were recorded in diffuse reflectance mode on a Nicolet 6700 FT-IR spectrometer, in an air-tight cell with CaF_2 windows under an atmosphere of Ar at room temperature. For X-ray absorption spectroscopy, samples were sent in sealed vials to the Stanford Synchrotron Radiation Lightsource (SSRL). High Resolution transmission electron microcopy (TEM) and Energy Dispersive X-ray (EDX) spectroscopy were performed at the Centre Technologique des Microsructures, Université Lyon 1. Prior to EDX/STEM/HRTEM analysis (JEOL 2100F, 200 kV), samples were prepared by placing a spot of a suspension containing the test material on an ultrathin Ni grid. Single crystal X-ray diffraction (XRD) was recorded at the Institut des Sciences Analytiques Lyon 1.

Electron paramagnetic resonance (EPR) spectroscopy was carried out with a Bruker spectrometer Elexsys E500 using X Band (9.4 GHz) radiation at T = 110–120 K, in the Laboratoire de Chimie, ENS Lyon. Samples for EPR were prepared in air-tight quartz tubes loaded inside a glove box. For quantitative studies of the paramagnetic phase, double integration of the EPR signal was performed and compared to that of a reference composed of a known amount of vanadyl(IV) sulfate. A Micromeritics ASAP 2020 (surface area and porosity analyzer) was used for the determination of textural properties (e.g., Brunauer-Emmett-Teller, B.E.T. surface area). Off-line gas chromatographic analyses were performed on an HP 5890 series II GC, equipped with an HP5 GC column and FID detector.

XAS spectra were acquired at ESRF, Grenoble, France, using BM23 beam-line at the iron K-edge in the transmission mode between 7.0 and 8.2 keV. Four scans were recorded at room temperature for each sample. Each data set was collected simultaneously with a Fe metal foil and was later aligned according to that reference (first inflection point set at 7112.0 eV). The samples were packed in an argon-filled glovebox within double air-tight sample holders. The data analyses were carried out using the program "Athena" [46] and the EXAFS fitting program "RoundMidnight", from the "MAX" package,[47] using spherical waves. For each neighboring atom or path i, the refined parameters are N_i, the number of neighbors; R_i(Å), the distance of the Fe center to that neighbor; σ_i^2 (Å^2), the Debye-Waller parameter; ΔE_0 (eV) designing the global energy shift. The program FEFF8 was used to calculate theoretical files for phases and amplitudes based on model clusters of atoms.[48]

2.3 Catalyst preparation

The molecular iron complex. [{(THF)$_2$KFe(O*t*Bu)$_3$}$_2$] was synthesized as reported in a recent work.[45]

Preparation of the supports.

Grafting of molecular complexes onto supports. As described most recently in the case of FeK on Al_2O_3,[45] a solution of [{(THF)$_2$KFe(O*t*Bu)$_3$}$_2$] (0.25 g) solution in n-pentane (15 mL) was added to 3 g $ZrO_{2\text{-}250}$ to produce a solid containing *ca.* 1 wt% Fe. The brownish suspension was stirred for 12 h at room temperature, then filtered through a glass frit. The solid was dried under high vacuum (10^{-5} mbar) while the filtrate was analyzed by GC. The same procedure was used to graft [{(THF)$_2$KFe(O*t*Bu)$_3$}$_2$] onto $SiO_{2\text{-}700}$, Al_2O_3-$MgO_{\text{-}500}$, $Nb_2O_{5\text{-}250}$, µ-ZSM-5_{250}, SiO_2-$Al_2O_{3\text{-}500}$, $CeO_{2\text{-}250}$ and $CeZrO_{2\text{-}250}$ (all *ca.* 1 wt% Fe).

2.4 Catalytic testing.

Catalysts were evaluated in a ½" stainless-steel tubular continuous flow reactor whose outlet was connected to an online GC-FID (Agilent Technologies 7890A). The dead volume was minimized using stainless steel inserts. The GC is equipped with two columns in series: GC a Carbon Plot column to separate CO_2, CO, and CH_4, and a PoraPlot Q column to separate higher hydrocarbons. The gas effluent from the reactor passes through both columns before reaching the detectors. Separated products were detected by thermal conductivity (TCD) and flame ionization (FID), connected in series. The FID is equipped with a Jetanizer^{TM} methanizer. The catalyst bed (250 mg) was charged in the glovebox and equipped with a 4-way valve, allowing

extensive purging of the gas lines with the reactant gas once connected to the reactor (PID, Micrometrics). The gas flow was controlled using Bronkhorst mass flow controllers. Catalytic tests were performed using a certified gas mixture with a H_2/CO_2 ratio of 3 (Mélange Crystal, Air Liquide), at a constant flow rate of 3 mL/min (measured at room temperature). Prior to starting the reaction, the catalyst was activated in situ in flowing Ar (Alphagaz 1, Air Liquide) for 2 h at 300 °C. CO_2 conversion and product selectivity were calculated using eq. 4 – 6.

$$Conversion\ (CO_2) = \frac{(CO_2)inlet - (CO_2)outlet}{(CO_2)inlet} \times 100\% \quad (4)$$

$$Selectivity\ to\ CO = \frac{(CO)outlet}{(CO_2)inlet - (CO_2)outlet} \times 100\% \quad (5)$$

$$Selectivity\ to\ CH_4 = \frac{(CH_4)outlet}{(CO_2)inlet - (CO_2)outlet} \times 100\% \quad (6)$$

3. Results and Discussion

3.1. Supported [{(THF)$_2$KFe(O*t*Bu)$_3$}$_2$] single site on $ZrO_{2\text{-}250}$ through surface organometallic chemistry

3.1.1. Preparation and characterization of ZrO_2 dehydroxylated at 250 °C ($ZrO_{2\text{-}250}$)

Commercial ZrO_2 was obtained from Sigma-Aldrich as white powder with a surface area of 80 m^2/g determined by BET using N_2 adsorption at 77 K (**Table S1**). After calcination at 550 °C for 24 hours and hydration at 100 °C with vapor, $ZrO_{2\text{-}250}$ was obtained by dehydroxylation at 250 °C for 12 hours. The surface area and pore volume of $ZrO_{2\text{-}250}$ support by N_2 adsorption at 77 K were found to be 72 m^2/g and 0.10cm^3/g respectively, these values are similar to the one reported in literature.[49-51] Furthermore, adsorption-desorption isotherm plot (**Figure S1** and **Table S2**) of the zirconia dehydroxylated at 250°C follows type IV adsorption-desorption isotherm which is similar to those already reported in literature.[51–53] Diffraction patterns of $ZrO_{2\text{-}250}$ is represented in **Figure S2** and shows a wide range of angle of 2θ from 18 to 65° corresponding to the presence of mainly monoclinic (baddeleyite), mixed with tetragonal phase based on the match search with the data of the Joint Committee on Power Diffraction Standards (JCPDS). This is similar to the diffraction patterns of ZrO_2 reported in literature.[54–56] Peaks at 2θ = 30.32°, 35.20°, 42.84°, 50.56°, 60.04°, 63.00 and 74.52° corresponding to XRD pattern of tetragonal phase and Peaks at 2θ = 24.5°, 28.20°,31.5°, 34.56°, 42.10°,46.5°, 50.50, and 66.04° corresponding to XRD pattern of baddeleyite phase.[57,58] The surface properties of the commercial ZrO_2 did not change after thermal treatment. This result was also supported by

Infrared spectroscopy where the spectrum of $ZrO_{2\text{-}250}$ obtained by Reflectance Infrared Fourier Transform spectroscopy (DRIFT) showed hydroxyl groups attributed to a mixture of tetragonal and monoclinic phase

In fact, different zirconia polymorphs possessed varied surface hydroxyl groups and acid-base properties.[59] Bi-bridged hydroxyl only existed on tetragonal zirconia and amorphous zirconia showed obvious H-band hydroxyl while two type of tri-bridged hydroxyl appeared on monoclinic zirconia.[59,60] These differences affected surface acidity and basicity: amorphous zirconia had strong Lewis acid sites and monoclinic zirconia had strong Brønsted acid sites, but for tetragonal zirconia, the basicity was predominant.[59,61,62] The DRIFT spectrum of $ZrO_{2\text{-}250}$ shows three main bands at 3774, 3738, and 3675 cm^{-1} assigned to the OH stretches of terminal, 2-fold coordinated (bi-bridged), and 3-fold coordinated (tri-bridged) hydroxyl groups, respectively (**Figure 1**a).[62–65] This spectrum is similar in situ DRIFT of ZrO_2 heated at different temperatures reported in literature.[65,66] The current spectrum is also in good agreement with the theoretical calculations in which terminal hydroxyls were found to vibrate between 3822 and 3743 cm^{-1}, bi-bridged hydroxyls in the range of 3755-3568 cm^{-1}, and tri-bridged hydroxyls between 3647 and 3498 cm^{-1}.[65–67] To achieve the grafting and functionalization of surface hydroxides under optimum conditions, their quantification is required. Among the different quantification methods, a chemical titration using $Al(iBu)_3$, a surface reaction with a highly reactive organometallic complex, has shown to be reliable.[68,69] This complex quantitatively reacts in pentane with surface hydroxyl groups of $ZrO_{2\text{-}500}$ by releasing one equivalent of isobutane per OH. The quantification of isobutane by GC shows that $ZrO_{2\text{–}250}$ contains 0.25 mmol OH g^{-1} that corresponds to 2.1 OH/nm^2.

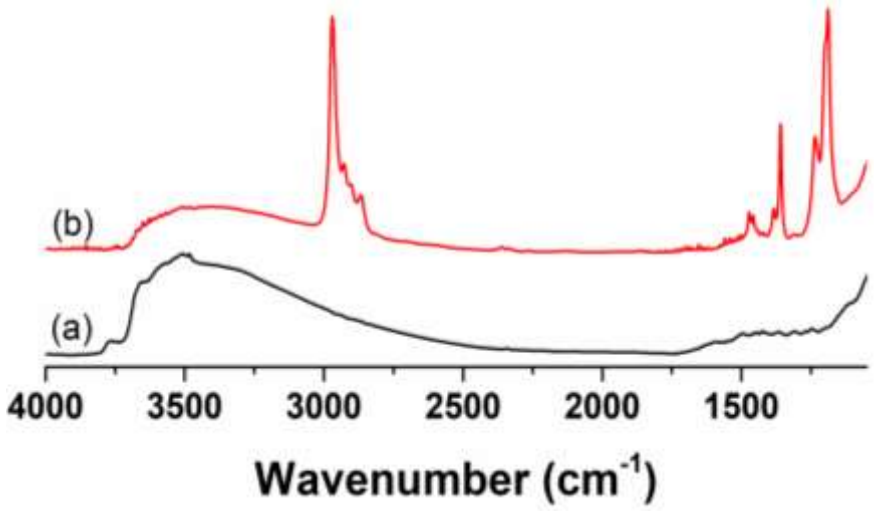

Figure 1. DRIFT spectra of **(a)** unmodified $ZrO_{2\text{-}250}$ and **(b)** after reaction of $[\{(THF)_2KFe(OtBu)_3\}_2]$ with $ZrO_{2\text{-}250}$ to give **$FeK/ZrO_{2\text{-}250}$**.

3.1.2. Preparation and characterization of the catalyst FeK/$ZrO_{2\text{-}250}$

The supported catalyst was prepared by grafting of [{$(THF)_2KFe(OtBu)_3$}$_2$] (Fe/OH = 0.7, 1.0 wt% Fe) from a pentane solution onto zirconia partially dehydroxylated at 250 °C ($ZrO_{2\text{-}250}$).[15] The reaction was allowed to proceed at room temperature for 12 h. The solid was washed with pentane and dried under vacuum, affording a yellowish material. Upon grafting, *t*BuOH and THF were released, and their identity confirmed by GC. The resulting material was characterized by DRIFT, elemental analysis, EDX, BET, EPR, XRD and XAFS. The DRIFT spectrum revealed that the surface OH groups of $ZrO_{2\text{-}200}$ (ν(O-H); 3795–3660 cm^{-1}) were almost completely consumed by the grafting reaction (**Figure 1**b). Simultaneously, bands corresponding to the organic ligands appeared at 3000–2800 cm^{-1} (ν(C-H)); 1466 and 1455 cm^{-1} (δ(CH_x)) and at 1380 and 1356 cm^{-1} (δ(CH_3)). The [{$(THF)_2KFe(OtBu)_3$}$_2$]@$ZrO_{2\text{-}250}$ material was further characterized for the determination of textural properties using N_2 adsorption at 77 K. The isotherm plot **Figure S1 and Table S2**) showed a decrease in both pore volume and surface area (0.07cm^3/g and 55.26 m^2/g respectively) compared to $ZrO_{2\text{-}250}$ (0.11 cm^3/g and 71.90 m^2/g). The decrease in textual properties (pore volume, pore size and surface area) after grafting of complex on $ZrO_{2\text{-}250}$ was as expected and previously reported.[70–77] The adsorption-desorption plot (type IV) did not change after grafting of the complex on $ZrO_{2\text{-}250}$. X ray diffraction patterns of **FeK/$ZrO_{2\text{-}250}$** (**Figure S2**) showed characteristic phases corresponding to monoclinic and tetragonal zirconia.

No crystalline phases in the composition of ZrO_2-supported Fe-O catalyst were observed with 1wt% iron loading (iron oxides) with no formation of iron particles (iron oxides XRD main peaks, 2θ, Cu $\lambda_{K\alpha}$: FeO at 36.1, <u>41.9</u> and 60.8°; Fe_3O_4 at 30.1, <u>35.5</u>, 57.1 and 62.7°; Fe_2O_3 at 24.1, <u>33.1</u>, <u>35.6</u>, 49.5, 54.0, 62.4 and 64.0). There is no visible difference between the diffraction patterns of the $ZrO_{2\text{-}250}$ support (**Figure S2**a) and the grafted material **FeK/$ZrO_{2\text{-}250}$** (**Figure S2**b). This result is similar to what was observed in the case of several metals supported catalysts with low metal loading.[78–81] The result indicated that the anionic iron complex was highly dispersed on the surface of $ZrO_{2\text{-}250}$ in agreement with HRTEM. This revealed that with very low average density of Fe on the surface of $ZrO_{2\text{-}250}$ (1.6 Fe/nm^2), the formation of iron clusters during the grafting at low temperature (25 °C) is limited.

Elemental analysis of the resulting material, **FeK/ZrO$_{2\text{-}250}$**, reveals Fe, K and C contents of 1.16 wt%, 0.86 wt% and 2.98 wt%, respectively, representing a Fe/K atomic of 1. The amount of grafted Fe, 0.208 mmol/g $ZrO_{2\text{-}250}$, represents a grafting stoichiometry (mol Fe/mol OH) of 0.75 in agreement with DRIFT spectrum of **FeK/ZrO$_{2\text{-}250}$** where most OH groups were consumed. Furthermore, the C/Fe ratio of 11.96 was consistent with the loss of one HO*t*Bu ligand per Fe and retention of one THF solvating K^+ (expected C/Fe: 12). Based on mass balance analysis the nature of the support appeared to have no effect on the reactivity of the FeK precursor and the resulting structure on $ZrO_{2\text{-}250}$ surface, **FeK/ZrO$_{2\text{-}250}$**, since a similar surface complex was also obtained on $Al_2O_{3\text{-}500}$, **FeK/Al$_2$O$_3$**.[45] The Fe/K ratio of 1 was also confirmed by EDX analysis. Moreover, the EDX mapping and spectrum (**Figure S3** indicates that Fe and K are uniformly dispersed on the surface. No agglomerated phases of Fe or K are observed by HRTEM (Figure S4).

Importantly, the oxidation state in **FeK/ZrO$_{2\text{-}250}$** is predominantly Fe(II), based on the EPR analysis (**Figure S5**). In fact, EPR spectroscopy of [{(THF)$_2$KFe(O*t*Bu)$_3$}$_2$]@$ZrO_{2\text{-}250}$ shows evidence for only a small amount of Fe(III) (< 0.02%). This small amount is probably due to traces of Fe(III) in the molecular complex [{(THF)$_2$KFe(OtBu)$_3$}$_2$].

The structure of **FeK/ZrO$_{2\text{-}250}$** was further studied by X-ray absorption fine structure (XAFS) spectroscopy at the Fe K-edge. The XANES of **FeK/ZrO$_{2\text{-}250}$** (**Figure S6**), shows a pre-edge at + 1.2 (± 0.2) eV from Fe(0) edge with a maximum normalized intensity of 0.10. This suggests that the Fe sites in the supported complex are in a distorted tetrahedral coordination with an iron oxidation state of +2,[82,83] as also revealed by EPR spectroscopy (**Figure S5**). The EXAFS curve fit for **FeK/ZrO$_{2\text{-}250}$** is displayed in **Figure 2**, with the resulting parameters in **Table 1** (left part, Fresh sample). The results are consistent with a Fe center in a distorted tetrahedral geometry, with *ca.* three oxygen atoms at 2.00(2) Å and one more at 2.35(3) Å. The shorter distance is in the range of Fe-OR bond lengths observed for [{(THF)$_2$KFe(O*t*Bu)$_3$}$_2$] molecular complex by XRD (average: 1.995 ± 0.09 Å),[45] the EXAFS distance resolution being *ca.* 0.13 Å ($\pi/2k_{max}$). The longer distance may be attributed to a surface oxygen either from a surface hydroxyl group (see **Scheme I**), or bridged between two surface Zr atoms. The fit could be further improved by including additional shells of back-scatterers, in particular, two C atoms at 3.04(4) Å, one K atom at 2.87(4) Å and *ca.* one Zr atom at 3.55(4) Å. However, there is no evidence for a well-defined Fe-Fe path (expected at *ca.* 3.3 Å in a dimer structure), despite attempts to include it in the model. Based on this fit, a proposed mononomeric structure for zirconia-supported **[{(THF)$_2$KFe(O*t*Bu)$_3$}$_2$]** is displayed in **Scheme 2**.

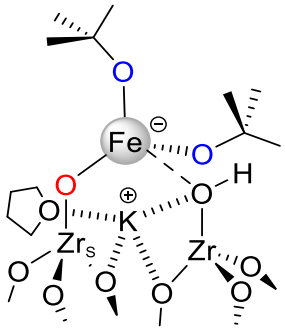

Scheme 2. Proposed monomeric structure for **FeK/ZrO$_{2\text{-}250}$**, prepared by grafting the dimeric complex [{(THF)$_2$KFe(O*t*Bu)$_3$}$_2$], **1**, onto ZrO$_{2\text{-}250}$. The structure is consistent with the XAFS analysis (the K coordination is proposed analogous to that of molecular complex **1**).

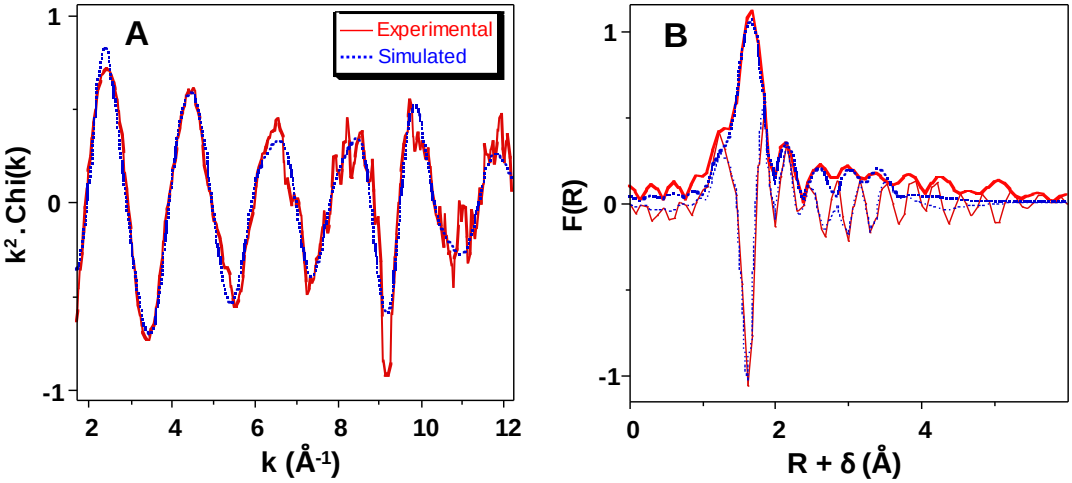

Figure 2. k^2-weighted Fe K-edge EXAFS of **FeK/ZrO$_{2\text{-}250}$**. **A**: *k*-space; **B**: R-space (FT modulus and imaginary part). Solid red lines: experimental data; dashed blue lines: curve fit obtained using spherical wave theory.

Table 1. EXAFS curve fit parameters for **FeK/ZrO$_{2\text{-}250}$** before and after catalytic reaction.[a]

	Fresh sample			After catalytic reaction		
Path	***N***	***R* (Å)**	**σ^2 (Å^2)**	***N***	***R* (Å)**	**σ^2 (Å^2)**
Fe-O$_1$(short)	2.7(5)	2.00(2)	0.0022(9)	2.9(5)	2.04(2)	0.0027(12)
Fe-O$_2$(long)	1.1(3)	2.35(3)	0.0022[b]	0.9(4)	2.34(3)	0.0027[b]
Fe--K	1.0	2.87(4)	0.0057(21)	1.0	2.90(4)	0.0084(20)
Fe--C / O	2.0	3.04(4)	0.0022(12)	1.9(6)	3.07(4)	0.0028(15)
Fe--Zr$_S$	0.9(3)	3.55(4)	0.0057[b]	1.8(7)	3.39(4)	0.0084[b]
	ΔE_0 = 6.4 ± 1.0 eV; ρ = 8.2 % $(\Delta\chi)^2/\nu$ = 2.47 (ν = 12 / 24)			ΔE_0 = 3.5 ± 0.9) eV; ρ = 6.4 % $(\Delta\chi)^2/\nu$ = 2.38 (ν = 10 / 23)		

[a] Errors generated by the EXAFS fitting program "RoundMidnight" are indicated in parentheses. Global fit parameter: S_0^2 = 0.93. Fresh sample: 1.7 ≤ k ≤ 12.2 Å^{-1}; 0.3 ≤ R ≤ 3.6 Å. Used sample: 1.7 ≤ k ≤ 12.1 Å^{-1}; 0.2 ≤ R ≤ 3.4 Å. Fit residual: ρ; Quality factor: $(\Delta\chi)^2/\nu$. [b] Shell constrained to a parameter above.

Overall, the evidence suggests that, in accordance with elemental analysis, the dimeric complex, [{(THF)$_2$KFe(OtBu)$_3$}$_2$], reacts readily with OH groups from zirconia by

protonolysis reaction, affording isolated, bipodal [(THF)K(Zr$_s$O)Fe(O*t*Bu)$_2$] species (**Scheme 3**). In this species, Fe is close to a K^+ counter-cation, and with a labile proton that may be located on a coordinated oxygen from the zirconia surface, as already reported on alumina.[45]

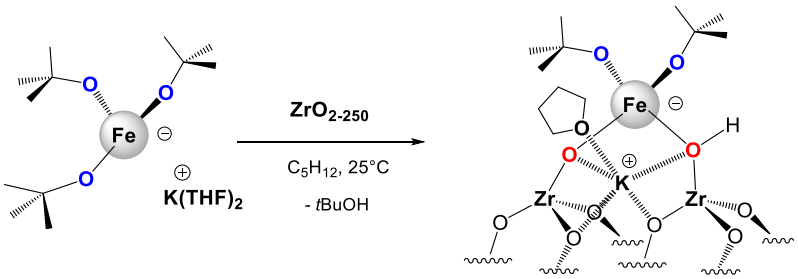

Scheme 3. Reaction of heterobimetallic [{(THF)$_2$KFe(OtBu)$_3$}$_2$] complex ZrO$_{2\text{-}250}$ to produce supported isolated single site [(THF)K(Zr$_s$O)Fe(O*t*Bu)$_2$] species.

3.1.3 Catalytic activity in CO_2 hydrogenation over FeK/ZrO$_{2\text{-}250}$

The RWGS activity and CO selectivity of catalyst, **FeK/ZrO$_{2\text{-}250}$**, was evaluated in a continuous flow reactor at 30 bar and 400 °C. The catalyst provided high CO_2 conversion (22 %, well below the equilibrium value of *ca.* 45% to ensure meaningful kinetic measurements) and selectivity towards CO (100%). This catalyst thus exhibited similar catalytic performance in terms of CO_2 conversion (22.5 %) and CO selectivity (100 %) than the Al$_2$O$_{3\text{-}500}$ counterpart recently reported (**Figure 3**b).[45]

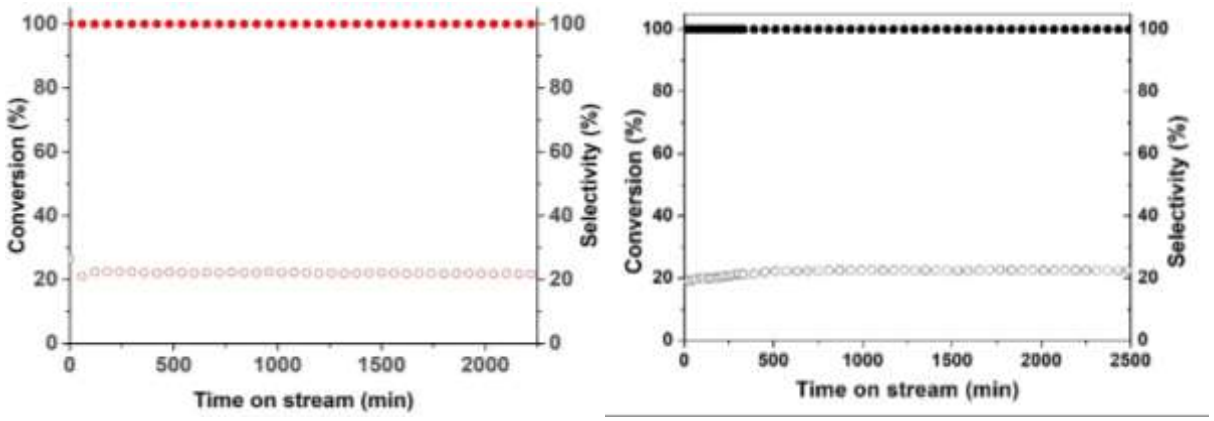

Figure 3. CO_2 conversion (open circles) and CO selectivity (filled circles) in the RWGS reaction catalyzed by (a) **FeK/ZrO$_{2\text{-}250}$** and (b) **FeK/Al$_2$O$_{3\text{-}500}$** (Feed composition: CO_2/H_2 = 1/3, volumetric flow rate = 3 mL min^{-1}, 400 °C, 30 bar).

No significant deactivation was observed over the course of 40 h (**Figure 4**). This high stability is likely due to the presence of well-dispersed isolated single sites, compared with a reported catalyst with a higher Fe loading that evolves to a material with a mixture of single sites and

nanoparticles.[84] The presence of K^+ in proximity to Fe appears to stabilize Fe(II), and provide a favorable site for CO_2 adsorption. EXAFS spectrum at the Fe K-edge of **FeK/ZrO$_{2\text{-}250}$** after a 40 h catalytic test is presented in **Figure 4** with the fit resulting parameters shown in **Table 1** (right part, After catalytic reaction). The coordination sphere of iron in sample **FeK/ZrO$_{2\text{-}250}$** after catalytic reaction is very similar to that in the fresh sample with iron single sites in a pseudo tetrahedral environment (ca. three oxygen atoms at 2.04(2) Å and one at 2.34(3) Å), a close K atom and grafted to the surface by ca. two Fe-OZr$_s$ bonds (**Scheme 4**). This result confirmed that no sintering or oxide phase occurred during the catalytic process.

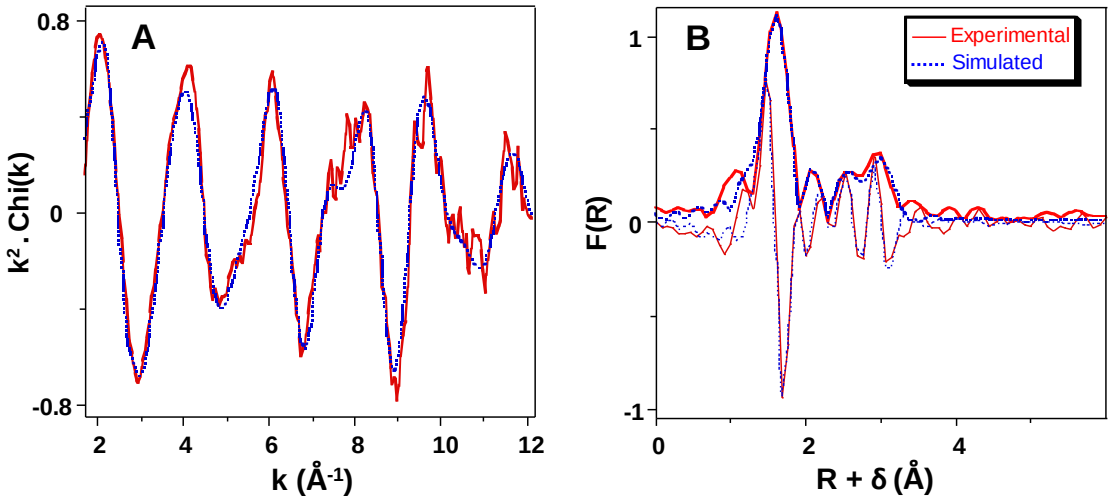

Figure 4. *k*^{2}-weighted Fe K-edge EXAFS of **FeK/ZrO$_{2\text{-}250}$** after catalytic reaction. **A**: *k*-space; **B**: R-space (FT modulus and imaginary part). Solid red lines: experimental data; dashed blue lines: curve fit obtained using spherical wave theory.

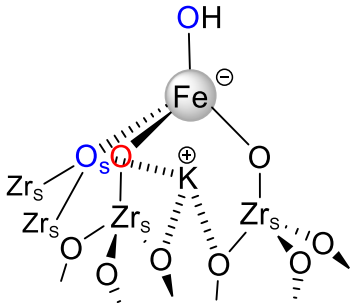

Scheme 4. Proposed monomeric structure for the iron site after catalytic reaction, consistent with the XAFS analysis.

In addition, HRTEM of **FeK/ZrO$_{2\text{-}250}$** performed after catalyst testing (**Figure S7**), supports the XAFS result showing that the active single site is robust under a range of reaction conditions. The presence of K^+ in proximity to Fe appears to stabilize Fe(II), and to provide a favorable site for CO_2 adsorption leading only to CO formation.

3.2. Preparation and characterization of other single site [{(THF)$_2$KFe(O*t*Bu)$_3$}$_2$] complex supported on different nature of oxide supports

This approach was extended to other oxide supports in order to study the effect of the acidity and redox properties on the catalytic performance of single site FeK catalysts. All the supports used in this study were pretreated at different temperatures to afford the given surface OH group concentration required for the grafting reaction of [{(THF)$_2$KFe(O*t*Bu)$_3$}$_2$]. **Table S1** describes the treatment conditions for each support. The supports were calcined in air at 500 °C followed by a dehydroxylation treatment and were denoted as $SiO_{2\text{-}700}$, Al_2O_3-$MgO_{\text{-}500}$, $Nb_2O_{5\text{-}250}$, µ-ZSM-5_{250}, SiO_2-$Al_2O_{3\text{-}500}$, $CeO_{2\text{-}250}$ and $CeZrO_{2\text{-}250}$ based on the dehydroxylation temperature used. The supported catalysts were all prepared by grafting [{(THF)$_2$KFe(O*t*Bu)$_3$}$_2$] in pentane solution for 12 h onto various pretreated supports with the same loading (1 $_{wt}$%Fe).[85,86] The resulting materials were then washed with pentane and dried under a high vacuum (10^{-4} mbar), affording yellowish powders (dark yellow for $CeO_{2\text{-}250}$), as reported in the case of [{(THF)$_2$KFe(O*t*Bu)$_3$}$_2$] supported alumina.[45] Upon grafting, *t*BuOH and THF were released as confirmed by GC analysis. The resulting supported materials, **FeK/$SiO_{2\text{-}700}$**, **FeK/Al_2O_3-$MgO_{\text{-}500}$**, **FeK/$Nb_2O_{5\text{-}250}$**, **FeK/µ-ZSM-$5_{\text{-}250}$**, **FeK/SiO_2-$Al_2O_{3\text{-}500}$**, **FeK/$CeO_{2\text{-}250}$** and **FeK/$CeZrO_{2\text{-}250}$**, were characterized by BET (**Table S2**), elemental analysis (**Table S3**), DRIFT, XRD, HRTEM/EDX, and EPR (see Supporting Information, **Figure S8-S18**). The results confirmed the successful grafting of the heterobimetallic [{(THF)$_2$KFe(O*t*Bu)$_3$}$_2$] complex via protonolysis of Fe-OtBu bonds by surface OH groups, as revealed by DRIFT and mass balance analysis. This leads to well dispersed Fe(II) mononuclear anionic surface species as shown by XRD, EPR, HRTEM and EDX (**Scheme 3**), similarly to what was observed in the case of $Al_2O_{3\text{-}500}$[45] and $ZrO_{2\text{-}250}$ with only a difference in the second neighbor, Si, Al, Zr or Ce.

3.3 Catalytic Activity of FeK on various supports in RWGS Reaction

The catalytic activity and CO selectivity of all [{(THF)$_2$KFe(O*t*Bu)$_3$}$_2$] supported materials were evaluated using a continuous-flow reactor at 30 bar and 400 °C. During each catalytic test, 250 mg of catalyst with a same 1 wt % Fe loading were introduced into the flow reactor. Prior to reaction, the catalysts were treated under Argon at 300°C for 150 min. The flow rate of CO_2 and H_2 mixture (1:3) was set at 3 mL min^{-1}, the temperature and pressure were ramped to the desired conditions (400°C and 30 bar). **Table 2** summarizes and compares the catalytic performances after 20 h on-stream for all catalysts during CO_2 hydrogenation. The catalytic performances as a function of time on stream are presented in **Figure S19-S20.** No significant

deactivation was observed for most catalysts (**FeK/$SiO_{2\text{-}700}$, FeK/$Al_2O_{3\text{-}500}$**, **FeK/$ZrO_{2\text{-}250}$**, **FeK/Al_2O_3-$MgO_{\text{-}500}$**, **FeK/SiO_2-$Al_2O_{3\text{-}500}$**, **FeK/µ-ZSM-$5_{\text{-}250}$** and **FeK/$Nb_2O_{5\text{-}250}$**) over the course of 40 h (**Figure S19-S20**). The high stability of these catalysts is likely due to the presence of well-dispersed isolated single sites and the presence of K^+ in proximity to Fe that stabilize Fe(II), and provide a favorable site for CO_2 adsorption.[43,45,84] However, the catalyst **FeK/$CeO_{2\text{-}250}$** showed an evolution of the stability as a function of time on stream.

Table 2. Catalytic performance of the different metal oxides supported materials during CO_2 hydrogenation under identical conditions.

	Catalyst	Conversion (%)	Selectivity (%)		
			CO	CH_4	C_2+
Neutral supports	**FeK/$Al_2O_{3\text{-}500}$**[45]	22.5	100		
	FeK/$SiO_{2\text{-}700}$	18	100	-	-
Basic supports	**FeK/Al_2O_3-$MgO_{\text{-}500}$**	17	100	-	-
	FeK/$ZrO_{2\text{-}250}$	22	100	-	-
Acidic supports	**FeK/SiO_2-$Al_2O_{3\text{-}500}$**	7.8	97	3	-
	FeK/µ-ZSM-$5_{\text{-}250}$	10	90	10	-
	FeK/$Nb_2O_{5\text{-}250}$	14	100	-	-
Redox supports	**FeK/$CeO_{2\text{-}250}$**	34	100 - 40	0 – 55	0 - 10
	FeK/$CeZrO_{2\text{-}250}$	26	100		-

Feed composition: CO_2/H_2 :1/3, flow = 3 ml.min^{-1}, 400 °C, 30 bars, amount = 250 mg

For acidic supports, the catalysts **FeK/SiO_2-$Al_2O_{3\text{-}500}$**, **FeK/µ-ZSM-$5_{\text{-}250}$** and **FeK/$Nb_2O_{5\text{-}250}$**, showed a lower CO_2 conversion compared to other supports (**Table 2**). The activity of these catalysts decreases when the acidic strength of the supports increases (**µ-ZSM-$5_{\text{-}250}$ > SiO_2-$Al_2O_{3\text{-}500}$ > $Nb_2O_{5\text{-}250}$**).[87–93] For the zeolite support, an ionic exchange process between a Brønsted proton and K^+ could have occurred during the catalysts preparation, as already reported for Fe/Y-zeolite and Co/ZSM-5 promoted by K.[94–96] This leads to a decrease of the amount of FeK active sites and a loss of the important K/Fe synergy for the RWGS reaction.[43,45] However, for neutral or basic supports ($Al_2O_{3\text{-}500}$, Al_2O_3-$MgO_{\text{-}500}$, $SiO_{2\text{-}700}$ or $ZrO_{2\text{-}250}$), no substantial support effect was observed in the RWGS reaction, with similar stable CO_2 conversion (with just minor variations) and high CO selectivities (100%). Therefore, the use of basic and neutral supports for single-site catalysts containing tailored potassium promoters

remains a promising strategy to tune the activity, selectivity and stability for RWGS. Interestingly, supports based on distinct elements such as Mg, Al, Si and Zr provide the same activity and selectivity in the RWGS reaction. This indicates that these elements contribute only to the dispersion and the stability of the active sites by keeping K^+ in proximity of Fe. This proximity may limit the sintering of Fe single site to Fe-NPs, generally known for methane formation.[94,95] This finding confirmed the critical role of K/Fe proximity in CO_2 adsorption and H_2 dissociation, as described in the previously proposed mechanism (**Scheme 1**) and supported by DFT calculations.[45] This is further validated by the use of ceria as a support. Indeed, when compared to acidic, neutral and basic supports, FeK supported on redox oxide $CeO_{2\text{-}250}$ showed a different behavior and underwent several evolutions during the time on stream. At initial time (**Figure 5**a), the conversion and the selectivity were similar to those obtained on neutral and basic supports (Conv. ca. 20 % and Sel. 100%) indicating that Fe and K are in proximity and the selective conversion of CO_2 to CO occurs in accordance with postulated mechanism without any contribution of ceria. After 200 min, a gradual decrease in CO selectivity by formation of methane accompanied by an increase in CO_2 conversion was observed (**Figure 5**a). This feature can be associated to an evolution of the RWGS active site (isolated anionic FeK) upon the feed exposure, in particular H_2. This is consistent with partial Fe agglomeration under the reaction conditions, resulting in small Fe NPs responsible for the methanation and light hydrocarbon production (C_2H_6 and C_3H_8).[96] Indeed, it is known that small Fe particles are more selective for methane during CO_2 reduction while catalysts with average particles size leads generally to light olefins and alkanes.[97,98] The agglomeration of Fe NPs is assumed to pursue until a steady state (after 1300 min), where the conversion (34%) and selectivities remained constant (CO = 38%; CH_4 = 54%; C_2-C_3 = 9%). The evolution of the selectivity in CO and methane during CO_2 conversion was already reported for Ru/Al_2O_3 where the authors observed the evolution of the active phase from Ru single site to Ru NPs using HRTEM and DRIFT during the RWGS reaction.[99] Another important example was reported in literature describing the CO_2 conversion by RWGS reaction on Ni supported on ceria with 1 % loading modified or unmodified by K^+.[100] This study suggests a K-guided selectivity control method based on the regulation of key intermediates HCO*/H_3CO* for Ni/CeO_2 catalysts. By incorporating K to Ni/CeO_2, the CO selectivity of CO_2 hydrogenation at 400 °C shifted from around 9 % for Ni/CeO_2 to approximately 85 % for Ni/CeO_2 promoted by K. The high stability of K-Ni/CeO_2 catalyst during the selective conversion of CO_2 to CO is attributed to the presence of excess of K (K/Ni ratio of 6) that limits the formation of nickel nanoparticles while keeping a K in proximity of each Ni. Importantly, Ang reported that at low loadings of Na (0.5 to 2 wt %), Na^+ was incorporated into the defective CeO_2 lattice,[101] generating a lattice strain and activating the lattice O_2, thereby increasing the reducibility of the catalyst. However, beyond the solubility limit of 2 wt %, Na deposited on the CeO_2 surface, retarding the reducibility and decreasing the activity in WGS.[101] Based on these findings, we propose a similar pathway in the case of $FeK/CeO_{2\text{-}250}$ where the evolution of the stability and selectivity during RWGS reaction may be explained by the incorporation of K^+ into $CeO_{2\text{-}250}$ lattice leading to the partial

loss of K in proximity of Fe. This Fe species without K could agglomerate over time in the presence of H_2 at 400 °C to form Fe NPs responsible for the formation of methane (**Scheme S1).** The evolution of the selectivity to CO and methane during the RWGS reaction could thus be correlated to the ratio of FeK single sites and Fe nanoparticles. The local structure of Fe on ceria before and after catalysis looked into using a combination of XRD and HRTEM analyses (**Figure S21 and S22**). However, due to the low loading of Fe, no Fe particles on ceria could be detected. Such limitations in XRD and HRTEM analysis were previously reported for Fe and Cu supported on CeO_2, where the XRD patterns and TEM images did not contain reflections related to Fe and Cu until the loadings exceeded 10 wt %, which is greater than the concentration of Fe in this study.[102–104] In addition, Fe K-edge X-ray spectroscopy of the catalysts FeK/$CeO_{2\text{-}250}$ before and after the catalytic tests could not lead to any significant changes due to the heavy absorption of Ce.[105] Furthermore, when the catalyst FeK/$CeO_{2\text{-}250}$ is reduced under hydrogen at a higher temperature (500 °C), the amount of the promotor, K, in the lattice of CeO_2 may increase and leads to an increase of Fe NPs on the surface and consequently a drop of the selectivity in CO from 45 % to 15 % due to the methanation reaction (**Figure 5)**. For comparison, FeK/$CeZrO_{x\text{-}250}$ was tested under the same conditions than FeK/$CeO_{2\text{-}250}$ in RWGS. Importantly, the catalyst FeK/$CeZrO_{x\text{-}250}$ showed high activity and stability over time of stream with high selectivity in CO (100 %) compared to FeK/$CeO_{2\text{-}250}$. This result in agreement with the explanation postulated above where the leaching of K in the lattice of Ceria in the case of FeK/ $CeO_{2\text{-}250}$ catalyst. This phenomenon is expected to be limited in the case of the FeK/$CeZrO_{x\text{-}250}$ catalyst, resulting in high selectivity and activity in RWGS reaction due to the synergy between Fe and K. Indeed, previous studies demonstrated that under reductive conditions, the structure of ceria-zirconia support is more stable than that of pure CeO_2. [106-108]

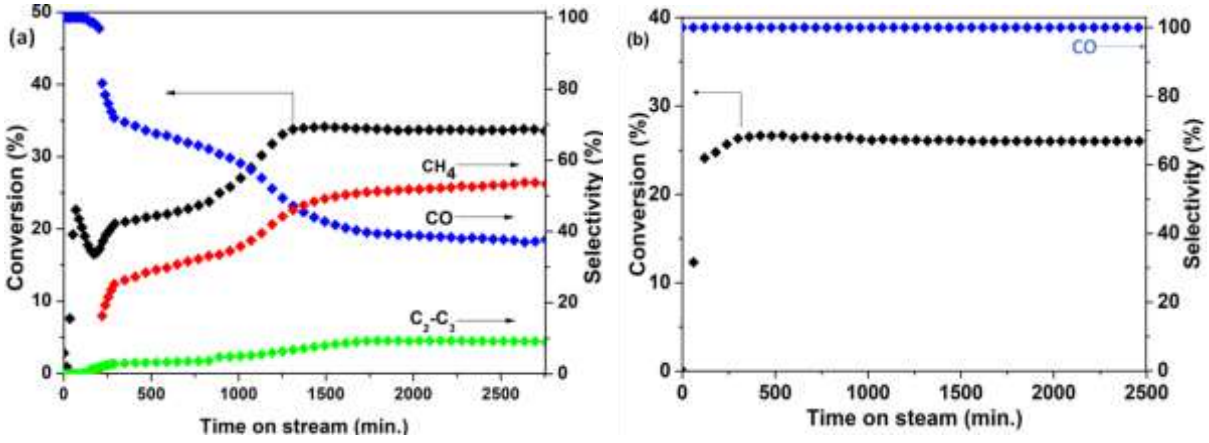

Figure 5. CO_2 conversion and products selectivity over (a) FeK/$CeO_{2\text{-}250}$ and (b) /FeKCeZr$O_{x\text{-}250}$ (Feed composition: CO_2/H_2 :1/3, flow = 3 ml.min^{-1}, 400 °C, 30 bars).

Therefore, all the results obtained supports the hypothesis that the reduction of CO_2 to CO is directed by the presence of K and Fe in proximity and that the supports contribute to the dispersion of the active phase. However, while neutral and basic supports had little influence on performance, ZrO_2 provided

the best results, maintaining high activity, selectivity, and long-term stability by preserving the Fe–K single site without agglomeration. In contrast, acidic supports degraded performance due to ion exchange disrupting Fe–K synergy, and CeO_2 caused Fe agglomeration and methane formation, though $CeZrO_2$ mitigated these issues. Mechanistic studies confirmed that the cooperative action between Fe(II) and nearby K^+ cations is key to the reaction, with the support's role being primarily to stabilize this active site. This work highlights the importance of support-controlled dispersion and stabilization of Fe–K sites for efficient CO_2-to-CO conversion

4. Conclusions

The heterobimetallic complex, $[\{(THF)_2KFe(OtBu)_3\}_2]$, is successfully grafted with 1 wt% Fe loading onto a variety of solid supports, encompassing a wide spectrum of surface chemistries: neutral (SiO_2 and Al_2O_3), basic (Al_2O_3-MgO and ZrO_2), acidic (SiO_2-Al_2O_3, µ-H-ZSM-5, and Nb_2O_5), and redox (CeO_2 and $CeZrO_x$) oxides. This is achieved via a synthetic strategy based on SOMC for the grafting of reactive species in a stable and well dispersed fashion. Regardless of the support used, the grafted complexes consistently retain a K/Fe ratio of 1, with Fe remaining in its +2 oxidation state. The potassium cations play a stabilizing role, ensuring that anionic Fe–K single sites remains atomically dispersed across the support surfaces. Comprehensive characterization by DRIFT, EPR, ICP, EDX, HRTEM, BET, XRD, and Fe K-edge XAFS (especially for the ZrO_2 supported sample) confirm these structural features.

Catalytic tests in the RWGS reaction reveal the critical influence of the support in tuning activity, selectivity, and long-term performances. On neutral and basic oxides, the catalytic behavior is similar, showing minor dependence on the support's properties. However, ZrO_2 stands out: **FeK/ZrO_2-250** demonstrates exceptional RWGS activity and stability. This is attributed to zirconia's unique ability to anchor and disperse Fe–K species without promoting aggregation or sintering. Postreaction analyses confirm this stability. HRTEM images show no signs of clustering even after 40 hours on stream, while EXAFS spectra reveal no Fe–Fe interactions, indicating that the local environment, defined by Fe–O, Fe–K, and Fe–Zr distances, remains similar throughout the reaction. In contrast, catalysts supported on acidic oxides (µ-ZSM-5, SiO_2–Al_2O_3, and Nb_2O_5) are far less effective. These materials likely suffer from ion exchange between K^+ and Bronsted acid sites, disrupting the subtle Fe–K synergy essential for catalysis. Redox-active CeO_2 initially exhibits promising CO selectivity, but this quickly declines due to structural changes by diffusion of K^+ into the ceria lattice and formation of Fe nanoparticles, as previously reported in the literature, shifting the selectivity toward methane. Interestingly, due to the presence of the ZrO_2 phase, the mixed oxide, $CeZrO_x$, overcomes this issue by offering a more stable framework, preserving both catalytic performance and selectivity. Mechanistically, the RWGS reaction is found to rely on a cooperative interaction between Fe(II) and K^+: Fe(II) facilitates H_2 and CO_2 activation, forming hydroxycarbonyl intermediates, while nearby K^+ promoted CO_2 adsorption and

transition state stabilization. Across all supports, this Fe–K cooperation, not the inherent properties of the oxide supports, is the principal driver of activity and CO selectivity. Thus, this study highlights the importance of pairing Fe(II) with K^+ at the atomic level and choosing the right precursor and support to preserve this synergy. This work offers valuable insight into designing robust, selective RWGS catalysts for CO_2 conversion under mild conditions. Importantly, such materials may easily be transformed into bifunctional catalysts by adding a Fischer–Tropsch (FT) active phase (for example, well-defined metallic nanoparticles based on Fe, Co or Ru), yielding hydrocarbons directly from CO_2 through consecutive

Author contributions

The manuscript was written through contributions of all authors. All authors have given approval to the final version of the manuscript. Abdulrahman Adamu Isah and Yahaya Nasiru, performed the synthesis and characterization of catalysts and testing of the catalysts. Fadila Hamachi and Jie Pan performed the synthesis and characterization of catalysts and testing of the catalysts based on Silica and ZSM-5. Pierre-Yves Dugas conducted the electron microscopy studies. All these tasks were carried out under the supervision of Kai C. Szeto for testing of the catalysts and Aimery De Mallmann for the characterization of materials; Mostafa Taoufik and Cyril Godard conceived the initial idea and designed the project.

Conflicts of interest

The authors declare that they have no known competing financial interests or personal relationships that could have appeared to influence the work reported in this study.

Data availability

The data supporting this article have been included as part of the supplementary information (SI): Supplementary information is available.

Acknowledgements

A.A.I. and N. Y. thanks the Petroleum Technology Development Fund(PTDF). A.d.M. thanks Olivier Mathon and Kiril Lomachenko for their help during the recording of the X-ray absorption spectra at ESRF, on beam line BM23 (Proposal IN-1134). J.P. acknowledges grant PID2021-128128NB-I00 funded by MICIU/AEI/10.13039/501100011033 and by "FEDER/UE" and the Generalitat de Catalunya (2021SGR00110).

Notes and References

[1] Bown RM, Joyce M, Zhang Q, Reina TR, Duyar MS. Identifying Commercial Opportunities for the Reverse Water Gas Shift Reaction. Energy Technol 2021;9:2100554. https://doi.org/10.1002/ente.202100554.
[2] Rommens KT, Saeys M. Molecular Views on Fischer–Tropsch Synthesis. Chem Rev 2023;123:5798–858. https://doi.org/10.1021/acs.chemrev.2c00508.
[3] Lin T, An Y, Yu F, Gong K, Yu H, Wang C, et al. Advances in Selectivity Control for Fischer–Tropsch Synthesis to Fuels and Chemicals with High Carbon Efficiency. ACS Catal 2022;12:12092–112. https://doi.org/10.1021/acscatal.2c03404.
[4] Ebrahimi P, Kumar A, Khraisheh M. A Review of CeO2 Supported Catalysts for CO2 Reduction to CO through the Reverse Water Gas Shift Reaction. Catalysts 2022;12:1101. https://doi.org/10.3390/catal12101101.
[5] Zhang R, Wang Y, Gaspard P, Kruse N. The oscillating Fischer-Tropsch reaction. Science 2023;382:99–103. https://doi.org/10.1126/science.adh8463.
[6] Buchenberg P, Addanki T, Franzmann D, Winkler C, Lippkau F, Hamacher T, et al. Global Potentials and Costs of Synfuels via Fischer–Tropsch Process. Energies 2023;16:1976. https://doi.org/10.3390/en16041976.
[7] Jones MP, Krexner T, Bismarck A. Repurposing Fischer-Tropsch and natural gas as bridging technologies for the energy revolution. Energy Convers Manag 2022;267:115882. https://doi.org/10.1016/j.enconman.2022.115882.
[8] Ahmad K, Upadhyayula S. Greenhouse gas CO_2 hydrogenation to fuels: A thermodynamic analysis. Environ Prog Sustain Energy 2019;38:98–111. https://doi.org/10.1002/ep.13028.
[9] Wolf A, Jess A, Kern C. Syngas Production via Reverse Water-Gas Shift Reaction over a Ni-Al_2 O_3 Catalyst: Catalyst Stability, Reaction Kinetics, and Modeling. Chem Eng Technol 2016;39:1040–8. https://doi.org/10.1002/ceat.201500548.
[10] Portillo E, Gandara-Loe J, Reina TR, Pastor-Pérez L. Is the RWGS a viable route for CO2 conversion to added value products? A techno-economic study to understand the optimal RWGS conditions. Sci Total Environ 2023;857:159394. https://doi.org/10.1016/j.scitotenv.2022.159394.
[11] Su X, Yang X, Zhao B, Huang Y. Designing of highly selective and high-temperature endurable RWGS heterogeneous catalysts: recent advances and the future directions. J Energy Chem 2017;26:854–67. https://doi.org/10.1016/j.jechem.2017.07.006.
[12] Hussain I, Jalil AA, Hassan NS, Hamid MYS. Recent advances in catalytic systems for CO2 conversion to substitute natural gas (SNG): Perspective and challenges. J Energy Chem 2021;62:377–407. https://doi.org/10.1016/j.jechem.2021.03.040.
[13] Hatta AH, Jalil AA, Hassan NS, Hamid MYS, Bahari MB, Aziz MA, et al. A comprehensive review on the advancements in catalyst regeneration strategies for enhanced reactivity in CO methanation. Mater Today Chem 2023;33:101743. https://doi.org/10.1016/j.mtchem.2023.101743.
[14] Fan WK, Tahir M. Recent trends in developments of active metals and heterogenous materials for catalytic CO2 hydrogenation to renewable methane: A review. J Environ Chem Eng 2021;9:105460. https://doi.org/10.1016/j.jece.2021.105460.
[15] Schmider D, Maier L, Deutschmann O. Reaction Kinetics of CO and CO_2 Methanation over Nickel. Ind Eng Chem Res 2021;60:5792–805. https://doi.org/10.1021/acs.iecr.1c00389.
[16] Kattel S, Yan B, Chen JG, Liu P. CO2 hydrogenation on Pt, Pt/SiO2 and Pt/TiO2: Importance of synergy between Pt and oxide support. J Catal 2016;343:115–26. https://doi.org/10.1016/j.jcat.2015.12.019.
[17] Zhu M, Ge Q, Zhu X. Catalytic Reduction of CO2 to CO via Reverse Water Gas Shift Reaction: Recent Advances in the Design of Active and Selective Supported Metal Catalysts. Trans Tianjin Univ 2020;26:172–87. https://doi.org/10.1007/s12209-020-00246-8.
[18] Chen X, Chen Y, Song C, Ji P, Wang N, Wang W, et al. Recent Advances in Supported Metal Catalysts and Oxide Catalysts for the Reverse Water-Gas Shift Reaction. Front Chem 2020;8:709. https://doi.org/10.3389/fchem.2020.00709.

[19] González-Castaño M, Dorneanu B, Arellano-García H. The reverse water gas shift reaction: a process systems engineering perspective. React Chem Eng 2021;6:954–76. https://doi.org/10.1039/D0RE00478B.
[20] Daza YA, Kuhn JN. CO_2 conversion by reverse water gas shift catalysis: comparison of catalysts, mechanisms and their consequences for CO_2 conversion to liquid fuels. RSC Adv 2016;6:49675–91. https://doi.org/10.1039/C6RA05414E.
[21] Liang B, Duan H, Su X, Chen X, Huang Y, Chen X, et al. Promoting role of potassium in the reverse water gas shift reaction on Pt/mullite catalyst. Catal Today 2017;281:319–26. https://doi.org/10.1016/j.cattod.2016.02.051.
[22] Kattel S, Yan B, Yang Y, Chen JG, Liu P. Optimizing Binding Energies of Key Intermediates for CO_2 Hydrogenation to Methanol over Oxide-Supported Copper. J Am Chem Soc 2016;138:12440–50. https://doi.org/10.1021/jacs.6b05791.
[23] Kwak JH, Kovarik L, Szanyi J. Heterogeneous Catalysis on Atomically Dispersed Supported Metals: CO_2 Reduction on Multifunctional Pd Catalysts. ACS Catal 2013;3:2094–100. https://doi.org/10.1021/cs4001392.
[24] Bobadilla LF, Santos JL, Ivanova S, Odriozola JA, Urakawa A. Unravelling the Role of Oxygen Vacancies in the Mechanism of the Reverse Water–Gas Shift Reaction by *Operando* DRIFTS and Ultraviolet–Visible Spectroscopy. ACS Catal 2018;8:7455–67. https://doi.org/10.1021/acscatal.8b02121.
[25] Lu B, Ju Y, Abe T, Kawamoto K. Dispersion and distribution of bimetallic oxides in SBA-15, and their enhanced activity for reverse water gas shift reaction. Inorg Chem Front 2015;2:741–8. https://doi.org/10.1039/C5QI00062A.
[26] Lu B, Kawamoto K. Preparation of monodispersed NiO particles in SBA-15, and its enhanced selectivity for reverse water gas shift reaction. J Environ Chem Eng 2013;1:300–9. https://doi.org/10.1016/j.jece.2013.05.008.
[27] Wang C, Guan E, Wang L, Chu X, Wu Z, Zhang J, et al. Product Selectivity Controlled by Nanoporous Environments in Zeolite Crystals Enveloping Rhodium Nanoparticle Catalysts for CO_2 Hydrogenation. J Am Chem Soc 2019;141:8482–8. https://doi.org/10.1021/jacs.9b01555.
[28] Biswas S, Kundu C, Kulkarni AP, Kattel S, Giddey S, Bhattacharya S. A Study on CO_2 Hydrogenation Using a Ceria–Zirconia Mixed Oxide ($Ce_x Zr_{1-x} O_2$)-Supported Fe Catalyst. Ind Eng Chem Res 2021;60:14410–23. https://doi.org/10.1021/acs.iecr.1c03044.
[29] Yan B, Zhao B, Kattel S, Wu Q, Yao S, Su D, et al. Tuning CO2 hydrogenation selectivity via metal-oxide interfacial sites. J Catal 2019;374:60–71. https://doi.org/10.1016/j.jcat.2019.04.036.
[30] Kattel S, Yu W, Yang X, Yan B, Huang Y, Wan W, et al. CO_2 Hydrogenation over Oxide-Supported PtCo Catalysts: The Role of the Oxide Support in Determining the Product Selectivity. Angew Chem Int Ed 2016;55:7968–73. https://doi.org/10.1002/anie.201601661.
[31] Kim SS, Lee HH, Hong SC. A study on the effect of support's reducibility on the reverse water-gas shift reaction over Pt catalysts. Appl Catal Gen 2012;423–424:100–7. https://doi.org/10.1016/j.apcata.2012.02.021.
[32] Nolan M, Parker SC, Watson GW. The electronic structure of oxygen vacancy defects at the low index surfaces of ceria. Surf Sci 2005;595:223–32. https://doi.org/10.1016/j.susc.2005.08.015.
[33] Lu B, Kawamoto K. Preparation of mesoporous CeO2 and monodispersed NiO particles in CeO2, and enhanced selectivity of NiO/CeO2 for reverse water gas shift reaction. Mater Res Bull 2014;53:70–8. https://doi.org/10.1016/j.materresbull.2014.01.043.
[34] Yoshihara J, Campbell CT. Methanol Synthesis and Reverse Water–Gas Shift Kinetics over Cu(110) Model Catalysts: Structural Sensitivity. J Catal 1996;161:776–82. https://doi.org/10.1006/jcat.1996.0240.
[35] Li H-J, Ho J-J. Density Functional Calculations on the Hydrogenation of Carbon Dioxide on Fe(111) and W(111) Surfaces. J Phys Chem C 2010;114:1194–200. https://doi.org/10.1021/jp909428r.
[36] Pahija E, Panaritis C, Gusarov S, Shadbahr J, Bensebaa F, Patience G, et al. Experimental and Computational Synergistic Design of Cu and Fe Catalysts for the Reverse Water–Gas Shift: A Review. ACS Catal 2022;12:6887–905. https://doi.org/10.1021/acscatal.2c01099.

[37] Li D, Ding X, Liu X, Cheng J, Jiang Z, Guo Y. CO2 hydrogenation to methane over Ni/ZrO2 and Ni/CeO2 catalysts: experimental and DFT studies. J Mater Sci 2023;58:12584–95. https://doi.org/10.1007/s10853-023-08814-8.
[38] Wang Z, Wang Q, Liao Y, Shen G, Gong X, Han N, et al. Comparative Study of CeO_2 and Doped CeO_2 with Tailored Oxygen Vacancies for CO Oxidation. ChemPhysChem 2011;12:2763–70. https://doi.org/10.1002/cphc.201100346.
[39] Yu Y, Xia W, Yu A, Simakov DSA, Ricardez-Sandoval L. Transition-Metal-Doped CeO_2 for the Reverse Water-Gas Shift Reaction: An Experimental and Theoretical Study on CO_2 Adsorption and Surface Vacancy Effects. ChemSusChem 2025;18:e202400681. https://doi.org/10.1002/cssc.202400681.
[40] Ebrahimi P, Kumar A, Khraisheh M. A Review of CeO2 Supported Catalysts for CO2 Reduction to CO through the Reverse Water Gas Shift Reaction. Catalysts 2022;12:1101. https://doi.org/10.3390/catal12101101.
[41] Zhu X, Shen M, Lobban LL, Mallinson RG. Structural effects of Na promotion for high water gas shift activity on Pt-Na/TiO2. J Catal 2011;278:123–32. https://doi.org/10.1016/j.jcat.2010.11.023.
[42] Yang M, Li S, Wang Y, Herron JA, Xu Y, Allard LF, et al. Catalytically active Au-O(OH)(x)-species stabilized by alkali ions on zeolites and mesoporous oxides. SCIENCE 2014;346:1498–501. https://doi.org/10.1126/science.1260526.
[43] Loiland JA, Wulfers MJ, Marinkovic NS, Lobo RF. Fe/γ-Al_2O_3 and Fe–K/γ-Al_2O_3 as reverse water-gas shift catalysts. Catal Sci Technol 2016;6:5267–79. https://doi.org/10.1039/C5CY02111A.
[44] Samantaray MK, D'Eia V, Pump E, Falivene L, Harb M, Chikh SO, et al. The Comparison between Single Atom Catalysis and Surface Organometallic Catalysis. Chem Rev 2020;120:734–813. https://doi.org/10.1021/acs.chemrev.9b00238.
[45] Isah AA, Ohiro O, Li L, Nasiru Y, Szeto KC, Dugas P-Y, et al. Selective Catalytic Reduction of CO_2 to CO by a Single-Site Heterobimetallic Iron–Potassium Complex Supported on Alumina. ACS Catal 2024;14:2418–28. https://doi.org/10.1021/acscatal.3c04989.
[46] B. Ravel and M. Newville, ATHENA , ARTEMIS , HEPHAESTUS : data analysis for X-ray absorption spectroscopy using IFEFFIT, J. Synchrotron Radiat., 2005, 12, 537–541. https://doi.org/10.1107/S0909049505012719.
[47] A. Michalowicz, J. Moscovici, D. Muller-Bouvet, K. Provost, MAX: Multiplatform Applications for XAFS, J. Phys. Conf. Ser., 2009, 190, 012034. https://doi.org/10.1088/1742-6596/190/1/012034.
[48] A. L. Ankudinov, B. Ravel, J. J. Rehr and S. D. Conradson, Real-space multiple-scattering calculation and interpretation of x-ray-absorption near-edge structure, Phys. Rev. B, 1998, 58, 7565–7576. https://doi.org/10.1103/PhysRevB.58.7565.
[49] Zou H, Lin YS. Structural and surface chemical properties of sol–gel derived TiO2–ZrO2 oxides. Appl Catal Gen 2004;265:35–42. https://doi.org/10.1016/j.apcata.2004.01.015.
[50] Dominguez J. M., Hernandez JL, Sandoval G. Surface and catalytic properties of Al2O3–ZrO2 solid solutions prepared by sol–gel methods. Appl Catal Gen 2000;197:119–30. https://doi.org/10.1016/S0926-860X(99)00542-6.
[51] Chareonlimkun A, Champreda V, Shotipruk A, Laosiripojana N. Catalytic conversion of sugarcane bagasse, rice husk and corncob in the presence of TiO2, ZrO2 and mixed-oxide TiO2–ZrO2 under hot compressed water (HCW) condition. Bioresour Technol 2010;101:4179–86. https://doi.org/10.1016/j.biortech.2010.01.037.
[52] D'Souza L, Suchopar A, Zhu K, Balyozova D, Devadas M, Richards RM. Preparation of thermally stable high surface area mesoporous tetragonal ZrO2 and Pt/ZrO2: An active hydrogenation catalyst. Microporous Mesoporous Mater 2006;88:22–30. https://doi.org/10.1016/j.micromeso.2005.08.020.
[53] Tel H, Altaş Y, Eral M, Sert Ş, Çetinkaya B, İnan S. Preparation of ZrO2 and ZrO2–TiO2 microspheres by the sol–gel method and an experimental design approach to their strontium adsorption behaviours. Chem Eng J 2010;161:151–60. https://doi.org/10.1016/j.cej.2010.04.053.

[54] Purohit RD, Saha S, Tyagi AK. Combustion synthesis of nanocrystalline ZrO2 powder: XRD, Raman spectroscopy and TEM studies. Mater Sci Eng B 2006;130:57–60. https://doi.org/10.1016/j.mseb.2006.02.041.
[55] Srinivasan R, Davis BH, Cavin OB, Hubbard CR. Crystallization and Phase Transformation Process in Zirconia: An in situ High-Temperature X-ray Diffraction Study. J Am Ceram Soc 1992;75:1217–22. https://doi.org/10.1111/j.1151-2916.1992.tb05560.x.
[56] Lopez D, Suwannakarn K, Bruce D, Goodwinjr J. Esterification and transesterification on tungstated zirconia: Effect of calcination temperature. J Catal 2007;247:43–50. https://doi.org/10.1016/j.jcat.2007.01.003.
[57] Zhao Y, Li W, Zhang M, Tao K. A comparison of surface acidic features between tetragonal and monoclinic nanostructured zirconia. Catal Commun 2002;3:239–45. https://doi.org/10.1016/S1566-7367(02)00089-4.
[58] Nikolajsen MT, Grivel J-C, Gaur A, Hansen LP, Baumgarten L, Schjødt NC, et al. Surface ZnO on zirconia is highly active for high temperature methanol synthesis. J Catal 2024;431:115389. https://doi.org/10.1016/j.jcat.2024.115389.
[59] Ma Z-Y, Yang C, Wei W, Li W-H, Sun Y-H. Surface properties and CO adsorption on zirconia polymorphs. J Mol Catal Chem 2005;227:119–24. https://doi.org/10.1016/j.molcata.2004.10.017.
[60] Kouva S, Honkala K, Lefferts L, Kanervo J. Review: monoclinic zirconia, its surface sites and their interaction with carbon monoxide. Catal Sci Technol 2015;5:3473–90. https://doi.org/10.1039/C5CY00330J.
[61] Zhao Y, Li W, Zhang M, Tao K. A comparison of surface acidic features between tetragonal and monoclinic nanostructured zirconia. Catal Commun 2002;3:239–45. https://doi.org/10.1016/S1566-7367(02)00089-4.
[62] Jung KT, Bell AT. The effects of synthesis and pretreatment conditions on the bulk structure and surface properties of zirconia. J Mol Catal Chem 2000;163:27–42. https://doi.org/10.1016/S1381-1169(00)00397-6.
[63] Korhonen ST, Airaksinen SMK, Bañares MA, Krause AOI. Isobutane dehydrogenation on zirconia-, alumina-, and zirconia/alumina-supported chromia catalysts. Appl Catal Gen 2007;333:30–41. https://doi.org/10.1016/j.apcata.2007.08.040.
[64] Bachiller-Baeza B, Rodriguez-Ramos I, Guerrero-Ruiz A. Interaction of Carbon Dioxide with the Surface of Zirconia Polymorphs. Langmuir 1998;14:3556–64. https://doi.org/10.1021/la970856q.
[65] Kaphan DM, Klet RC, Perras FA, Pruski M, Yang C, Kropf AJ, et al. Surface Organometallic Chemistry of Supported Iridium(III) as a Probe for Organotransition Metal–Support Interactions in C–H Activation. ACS Catal 2018;8:5363–73. https://doi.org/10.1021/acscatal.8b00855.
[66] Korhonen ST, Calatayud M, Krause AOI. Structure and Stability of Formates and Carbonates on Monoclinic Zirconia: A Combined Study by Density Functional Theory and Infrared Spectroscopy. J Phys Chem C 2008;112:16096–102. https://doi.org/10.1021/jp803353v.
[67] Korhonen ST, Calatayud M, Krause AOI. Stability of Hydroxylated (1̄11) and (1̄01) Surfaces of Monoclinic Zirconia: A Combined Study by DFT and Infrared Spectroscopy. J Phys Chem C 2008;112:6469–76. https://doi.org/10.1021/jp8008546.
[68] Mazoyer E, Trébosc J, Baudouin A, Boyron O, Pelletier J, Basset J, et al. Heteronuclear NMR Correlations To Probe the Local Structure of Catalytically Active Surface Aluminum Hydride Species on γ-Alumina. Angew Chem Int Ed 2010;49:9854–8. https://doi.org/10.1002/anie.201004310.
[69] Larabi C, Chen C, Merle N, Charlin M, Szeto KC, De Mallmann A, et al. Well-defined surface tungstenocarbyne complex through the reaction of [W(□C *t* Bu)(CH_2 *t* Bu)$_3$] with CeO_2 : a highly stable precatalyst for NOx reduction with NH_3. New J Chem 2021;45:12024–32. https://doi.org/10.1039/D0NJ02146F.
[70] Idriss H, Diagne C, Hindermann JP, Kiennemann A, Barteau MA. Reactions of Acetaldehyde on CeO2 and CeO2-Supported Catalysts. J Catal 1995;155:219–37. https://doi.org/10.1006/jcat.1995.1205.

[71] Bickford ES, Velu S, Song C. Nano-structured CeO2 supported Cu-Pd bimetallic catalysts for the oxygen-assisted water–gas-shift reaction. Catal Today 2005;99:347–57. https://doi.org/10.1016/j.cattod.2004.10.010.
[72] Fox EB, Velu S, Engelhard MH, Chin Y-H, Miller JT, Kropf J, et al. Characterization of CeO2-supported Cu–Pd bimetallic catalyst for the oxygen-assisted water–gas shift reaction. J Catal 2008;260:358–70. https://doi.org/10.1016/j.jcat.2008.08.018.
[73] Choung SY, Ferrandon M, Krause T. Pt-Re bimetallic supported on CeO2-ZrO2 mixed oxides as water–gas shift catalysts. Catal Today 2005;99:257–62. https://doi.org/10.1016/j.cattod.2004.10.002.
[74] Sakpal T, Lefferts L. Structure-dependent activity of CeO2 supported Ru catalysts for CO2 methanation. J Catal 2018;367:171–80. https://doi.org/10.1016/j.jcat.2018.08.027.
[75] Nguyen HTT, Kumabe Y, Ueda S, Kan K, Ohtani M, Kobiro K. Highly durable Ru catalysts supported on CeO2 nanocomposites for CO2 methanation. Appl Catal Gen 2019;577:35–43. https://doi.org/10.1016/j.apcata.2019.03.011.
[76] Zhang S, Kim T. Effects of iron precursor and loading on the catalytic performance of FeOx/CeO2 catalysts for NO reduction by CO. Mol Catal 2020;494:111123. https://doi.org/10.1016/j.mcat.2020.111123.
[77] Qi X, Flytzani-Stephanopoulos M. Activity and Stability of Cu−CeO_2 Catalysts in High-Temperature Water−Gas Shift for Fuel-Cell Applications. Ind Eng Chem Res 2004;43:3055–62. https://doi.org/10.1021/ie0306170.
[78] Ebert DYu, Dorofeeva NV, Savel'eva AS, Kharlamova TS, Salaev MA, Svetlichnyi VA, et al. Silica-supported Fe-Mo-O catalysts for selective oxidation of propylene glycol. Catal Today 2019;333:133–9. https://doi.org/10.1016/j.cattod.2018.07.029.
[79] Das SK, Majhi S, Mohanty P, Pant KK. CO-hydrogenation of syngas to fuel using silica supported Fe–Cu–K catalysts: Effects of active components. Fuel Process Technol 2014;118:82–9. https://doi.org/10.1016/j.fuproc.2013.08.014.
[80] Maia MP, Rodrigues MA, Passos FB. Nitrate catalytic reduction in water using niobia supported palladium–copper catalysts. Catal Today 2007;123:171–6. https://doi.org/10.1016/j.cattod.2007.01.051.
[81] Chary KVR, Seela KK, Sagar GV, Sreedhar B. Characterization and Reactivity of Niobia Supported Copper Oxide Catalysts. J Phys Chem B 2004;108:658–63. https://doi.org/10.1021/jp035738s.
[82] Galoisy L, Calas G, Arrio MA. High-resolution XANES spectra of iron in minerals and glasses: structural information from the pre-edge region. Chem Geol 2001;174:307–19. https://doi.org/10.1016/S0009-2541(00)00322-3.
[83] Westre TE, Kennepohl P, DeWitt JG, Hedman B, Hodgson KO, Solomon EI. A Multiplet Analysis of Fe K-Edge 1s → 3d Pre-Edge Features of Iron Complexes. J Am Chem Soc 1997;119:6297–314. https://doi.org/10.1021/ja964352a.
[84] Loiland JA, Wulfers MJ, Marinkovic NS, Lobo RF. Fe/gamma-Al2O3 and Fe-K/gamma-Al2O3 as reverse water-gas shift catalysts. Catal Sci Technol 2016;6:5267–79. https://doi.org/10.1039/c5cy02111a.
[85] Szeto KC, Jones ZR, Merle N, Rios C, Gallo A, Le Quemener F, et al. A Strong Support Effect in Selective Propane Dehydrogenation Catalyzed by Ga(*i* -Bu)$_3$ Grafted onto γ-Alumina and Silica. ACS Catal 2018;8:7566–77. https://doi.org/10.1021/acscatal.8b00936.
[86] Basset J, Psaro R, Roberto D, Ugo R, editors. Modern Surface Organometallic Chemistry. 1st ed. Wiley; 2009. https://doi.org/10.1002/9783527627097.
[87] Paulis M, Martín M, Soria DB, Díaz A, Odriozola JA, Montes M. Preparation and characterization of niobium oxide for the catalytic aldol condensation of acetone. Appl Catal Gen 1999;180:411–20. https://doi.org/10.1016/S0926-860X(98)00379-2.
[88] Faba L, Gancedo J, Quesada J, Diaz E, Ordóñez S. One-Pot Conversion of Acetone into Mesitylene over Combinations of Acid and Basic Catalysts. ACS Catal 2021;11:11650–62. https://doi.org/10.1021/acscatal.1c03095.
[89] Reif P, Gupta NK, Rose M. Highly stable amorphous silica-alumina catalysts for continuous bio-derived mesitylene production under solvent-free conditions. Green Chem 2023;25:1588–96. https://doi.org/10.1039/D2GC04116B.

[90] Pieta IS, Ishaq M, Wells RPK, Anderson JA. Quantitative determination of acid sites on silica–alumina. Appl Catal Gen 2010;390:127–34. https://doi.org/10.1016/j.apcata.2010.10.001.
[91] Kotrel S, Rosynek MP, Lunsford JH. Quantification of Acid Sites in H-ZSM-5, H-β, and H-Y Zeolites. J Catal 1999;182:278–81. https://doi.org/10.1006/jcat.1998.2339.
[92] Borade R, Sayari A, Adnot A, Kaliaguine Serge. Characterization of acidity in ZSM-5 zeolites: an x-ray photoelectron and IR spectroscopy study. J Phys Chem 1990;94:5989–94. https://doi.org/10.1021/j100378a068.
[93] Wachs IE, Jehng J-M, Ueda W. Determination of the Chemical Nature of Active Surface Sites Present on Bulk Mixed Metal Oxide Catalysts. J Phys Chem B 2005;109:2275–84. https://doi.org/10.1021/jp048839e.
[94] Riedel T, Claeys M, Schulz H, Schaub G, Nam S-S, Jun K-W, et al. Comparative study of Fischer–Tropsch synthesis with H2/CO and H2/CO2 syngas using Fe- and Co-based catalysts. Appl Catal Gen 1999;186:201–13. https://doi.org/10.1016/S0926-860X(99)00173-8.
[95] Liu R, Leshchev D, Stavitski E, Juneau M, Agwara JN, Porosoff MD. Selective hydrogenation of CO2 and CO over potassium promoted Co/ZSM-5. Appl Catal B Environ 2021;284:119787. https://doi.org/10.1016/j.apcatb.2020.119787.
[96] Qin K, Men Y, Liu S, Wang J, Li Z, Tian D, et al. Direct conversion of carbon dioxide to liquid hydrocarbons over K-modified CoFeOx/zeolite multifunctional catalysts. J CO2 Util 2022;65:102208. https://doi.org/10.1016/j.jcou.2022.102208.
[97] Franken T, Heel A. Are Fe based catalysts an upcoming alternative to Ni in CO2 methanation at elevated pressure? J CO2 Util 2020;39:101175. https://doi.org/10.1016/j.jcou.2020.101175.
[98] Xie T, Wang J, Ding F, Zhang A, Li W, Guo X, et al. CO 2 hydrogenation to hydrocarbons over alumina-supported iron catalyst: Effect of support pore size. J CO2 Util 2017;19:202–8. https://doi.org/10.1016/j.jcou.2017.03.022.
[99] Kwak JH, Kovarik L, Szanyi J. CO_2 Reduction on Supported Ru/Al_2O_3 Catalysts: Cluster Size Dependence of Product Selectivity. ACS Catal 2013;3:2449–55. https://doi.org/10.1021/cs400381f.
[100] Zang Y, Zhang Z, Qu J, Gao F, Gu J, Wei T, et al. K-guided selective regulation mechanism for CO2 hydrogenation over Ni/CeO2 catalyst. J Colloid Interface Sci 2024;658:167–78. https://doi.org/10.1016/j.jcis.2023.12.025.
[101] Ang ML, Oemar U, Saw ET, Mo L, Kathiraser Y, Chia BH, et al. Highly Active Ni/ *x* Na/CeO_2 Catalyst for the Water–Gas Shift Reaction: Effect of Sodium on Methane Suppression. ACS Catal 2014;4:3237–48. https://doi.org/10.1021/cs500915p.
[102] Gou Z, Huang C, Zhou G, Ren X, Deng L, Wang T, et al. Coupling and electronic synergistic effects of Fe/CeO2 composite to achieve high efficiency and selectivity for RWGS reaction. J CO2 Util 2024;81:102728. https://doi.org/10.1016/j.jcou.2024.102728.
[103] Peck TC, Reddy GK, Jones M, Roberts CA. Monolayer Detection of Supported Fe and Co Oxides on Ceria To Establish Structure–Activity Relationships for Reduction of NO by CO. J Phys Chem C 2017;121:8435–43. https://doi.org/10.1021/acs.jpcc.7b00398.
[104] Sakai M, Nagai Y, Aoki Y, Takahashi N. Investigation into the catalytic reduction of NO at copper–ceria interface active sites. Appl Catal Gen 2016;510:57–63. https://doi.org/10.1016/j.apcata.2015.11.007.
[105] Gili A, Bekheet MF, Thimm F, Bischoff B, Geske M, Konrad M, et al. One-pot synthesis of iron-doped ceria catalysts for tandem carbon dioxide hydrogenation. Catal Sci Technol 2024;14:4174–86. https://doi.org/10.1039/D4CY00439F.
[106] Zhang C, Wen X-D, Teng B-T, Zhao Y, Fan M. Catalytic effects of Zr doping ion on ceria-based catalyst. Fuel Process Technol 2015;131:1–6. https://doi.org/10.1016/j.fuproc.2014.11.010.
[107] Zeng S, Zhang X, Fu X, Zhang L, Su H, Pan H. Co/CexZr1−xO2 solid-solution catalysts with cubic fluorite structure for carbon dioxide reforming of methane. Appl Catal B Environ 2013;136–137:308–16. https://doi.org/10.1016/j.apcatb.2013.02.019.
[108] Yu Q, Liu L, Dong L, Li D, Liu B, Gao F, et al. Effects of Ce/Zr ratio on the reducibility, adsorption and catalytic activity of CuO/CexZr1−xO2/γ-Al2O3 catalysts for NO reduction by CO. Appl Catal B Environ 2010;96:350–60. https://doi.org/10.1016/j.apcatb.2010.02.032.

Supporting Information

Table S1. The list of oxide supports and the pretreatment condition used

Support	Source	Purity (%)	Surface area (m^2/g)	Cal. (°C)	Dehydrox. (°C)	Denoted name
Fumed silica (Aerosil 200)	Evonik	99	200±25	N/A	700	$SiO_{2\text{-}700}$
Pural MG50	Sasol	50:50	200	500	500	Al_2O_3-$MgO_{\text{-}500}$
$Zr(OH)_4$	SIGMA	97	80	550	250	$ZrO_{2\text{-}250}$
Mesopourous N_2O_5-HY-340	CBMM	90	340	500	250	$Nb_2O_{5\text{-}250}$
silica-alumina HA-S-HPV	Azko-Nobel	75:25	N/A	500	500	$SiO\text{-}Al_2O_{3\text{-}500}$
µ-HZSM-5	Oslo	N/A	196	500	500	µ-$HZSM\text{-}5_{250}$
CeO_2	SOLVAY	(≥ 99.6	235	600	250	$CeO_{2\text{-}250}$
CeO_2:ZrO_2	SOLVAY	58:42	111	500	250	$CeZrO_{x\text{-}250}$

Table S2. Textural properties of the dehydroxylated support before and after grafting reaction using N_2 adsorption at 77K.

Material	**Surface area (m^2/g)**		**Pore volume (cm^3/g)**		**Pore size (nm)**		**Type of isotherm**
	a	**b**	**a**	**B**	**a**	**b**	
FeK/$SiO_{2\text{-}700}$	187	178	1.59	1.44	28.9	26.9	II
FeK/Al_2O_3-MgO_{500}	212	136	0.29	0.20	4.86	4.52	IV
FeK/$ZrO_{2\text{-}250}$	72	55	0.11	0.07	5.1	4.4	IV
FeK/SiO_2-$Al_2O_{3\text{-}500}$	408	346	1.15	0.79	8.22	7.05	IV
FeK/µ-ZSM-5	196	127	1.0	0.1	3.5	5.2	I
FeK/$Nb_2O_{5\text{-}250}$	40	38	0.15	0.14	10.8	10.5	IV
FeK/$CeO_{2\text{-}250}$	176	146	0.21	0.17	3.47	3.66	IV
FeK/CeZrOx$_{\text{-}250}$	94	63	0.25	0.17	7.5	6.67	IV

a- Dehydroxylated support **b-** [{(O*t*Bu)$_3$FeK(THF)}$_2$] complex grafted onto the support.

Table S3. Result of elemental analysis of [{(THF)$_2$KFe(O*t*Bu)$_3$}$_2$] grafted on different nature of oxide support.

Material	Elemental analysis (wt%)			K/Fe	C/Fe	Amount of Fe (mmol/gFe)
	Fe	K	C			
FeK/SiO$_{2\text{-}700}$	1.30	0.92	3.40	1.01	12.17	0.232
FeK/Al$_2$O$_3$-MgO$_{500}$	1.13	1.01	4.01	1.27	16.51	0.202
FeK/ZrO$_{2\text{-}250}$	1.16	0.86	2.98	1.06	11.95	0.208
FeK/SiO$_2$-Al$_2$O$_{3\text{-}500}$	1.34	1.03	3.42	1.09	11.87	0.239
FeK/µ-ZSM-5	1.39	1.02	3.54	1.05	11.85	0.249
FeK/Nb$_2$O$_{5\text{-}250}$	1.12	0.80	2.91	1.02	12.09	0.201
FeK/CeO$_{2\text{-}250}$	1.05	0.80	3.10	1.08	13.73	0.188
FeK/CeZrO$_{x\text{-}250}$	0.97	0.74	2.44	1.09	11.69	0.174

Expected value of K/Fe = 1 and C/Fe = 12

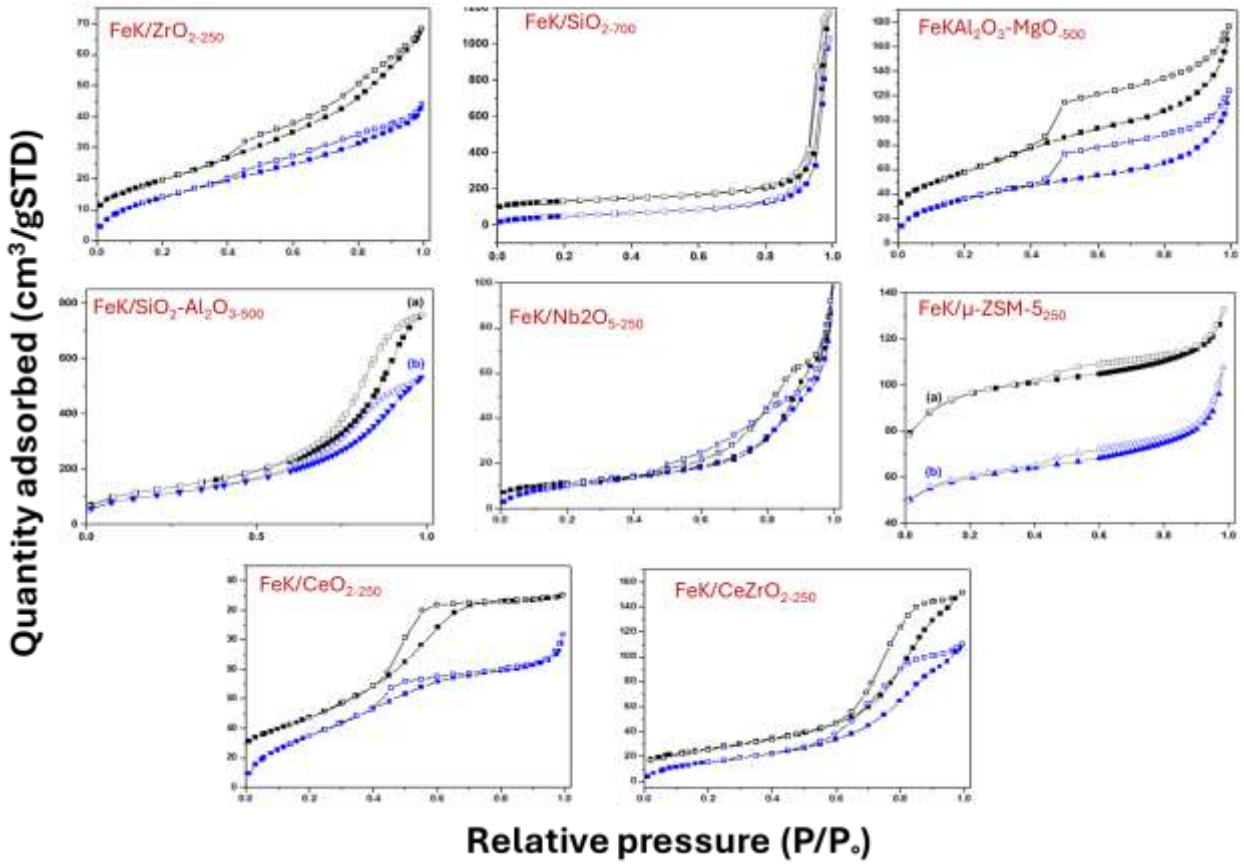

Fig. S1. N_2 adsorption/desorption isotherms at 77K of dehydroxylated supports (black) and of [{Fe(O*t*Bu)$_3$K(THF)$_2$] grafted onto different nature of supports (blue). Adsorption isotherms (full bullets) and desorption isotherms (empty bullets).

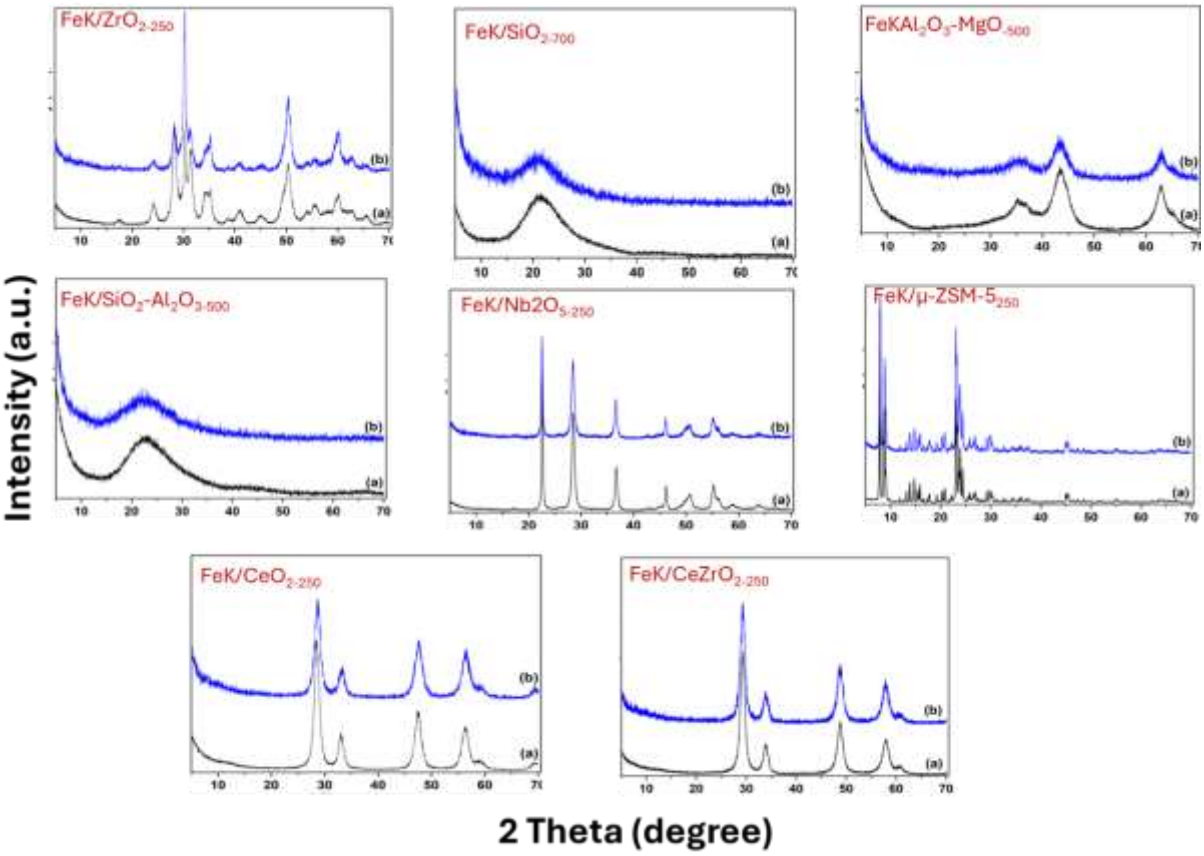

Fig. S2. X ray diffraction patterns of (a) dehydroxylated supports and (b) [{(THF)$_2$KFe(O*t*Bu)$_3$}] complex grafted onto different nature of supports.

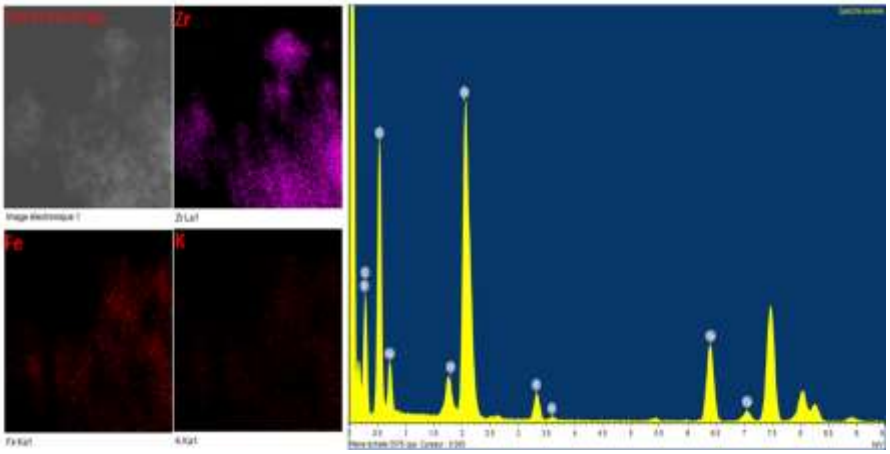

Fig. S3. EDX mapping (left) EDX spectrum (right) of **FeK/ZrO$_{2\text{-}250}$** (1wt% Fe loading).

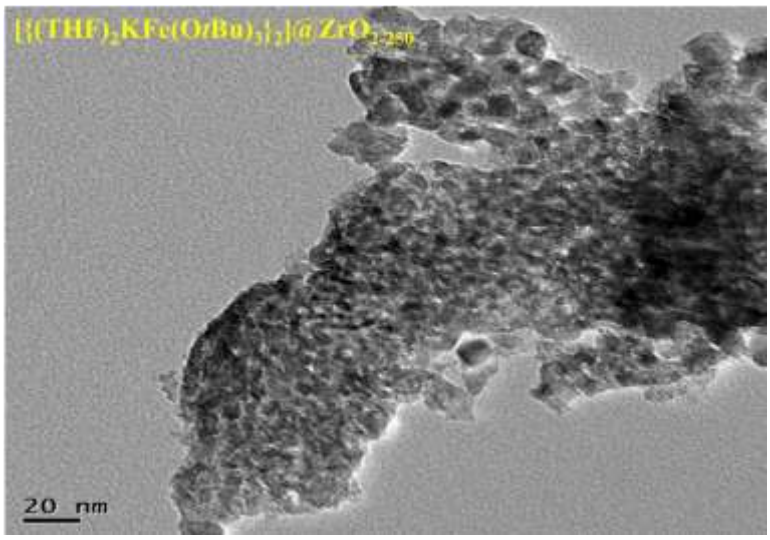

Fig. S4. HRTEM image of **FeK/ZrO$_{2\text{-}250}$ (**1wt% Fe loading).

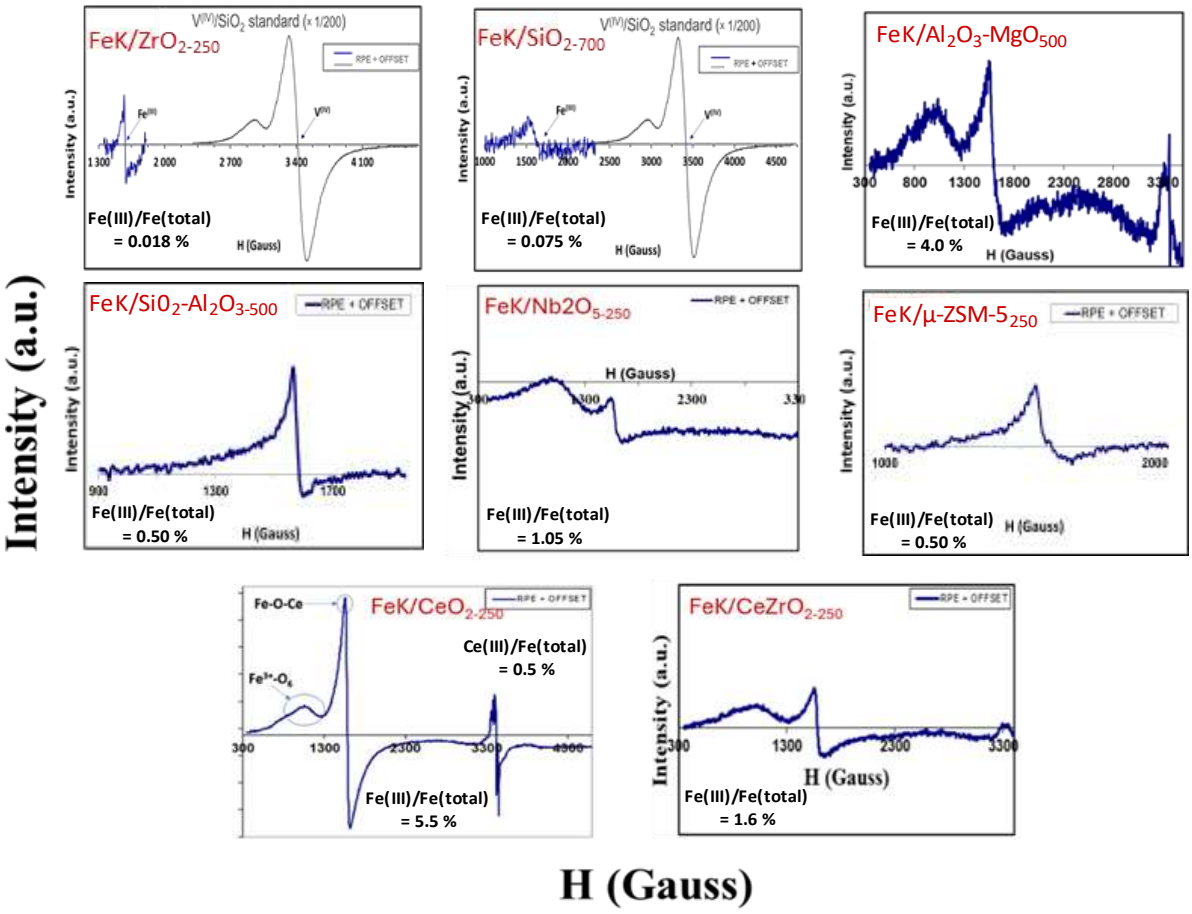

Fig. S5. EPR spectra of heterobimetallic [{(THF)$_2$KFe(O*t*Bu)$_3$}$_2$] complex grafted on different nature of supports.

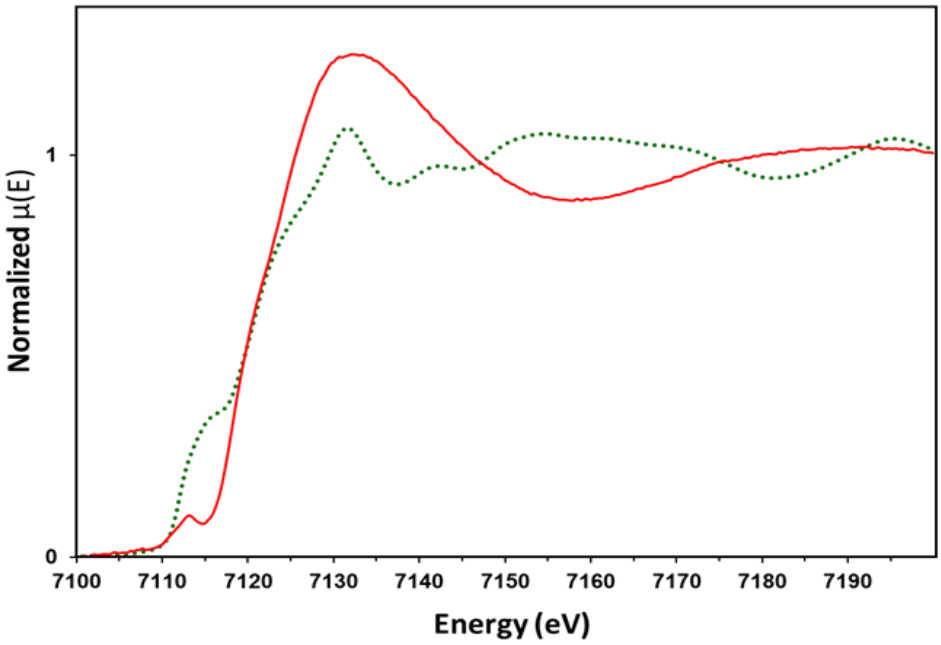

Fig. S6. XANES spectrum of **FeK/ZrO$_{2\text{-}250}$** (red line), with the spectrum of an iron foil shown for comparison (dashed green line).

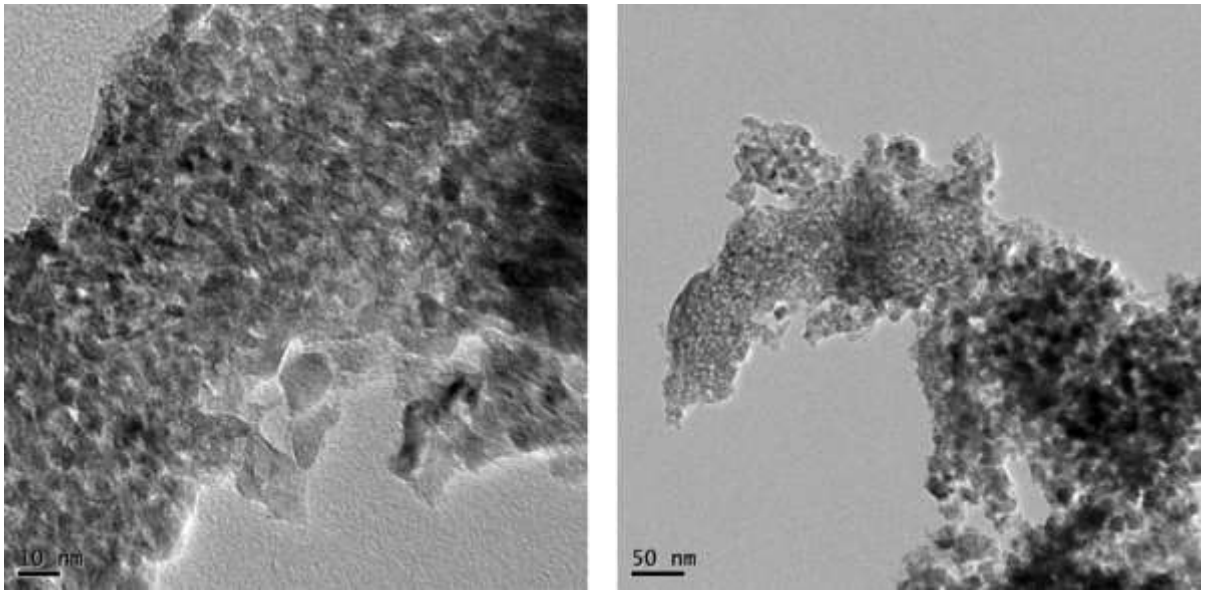

Fig. S7. HRTEM image of **FeK/ZrO$_{2\text{-}250}$** after 40h catalytic test.

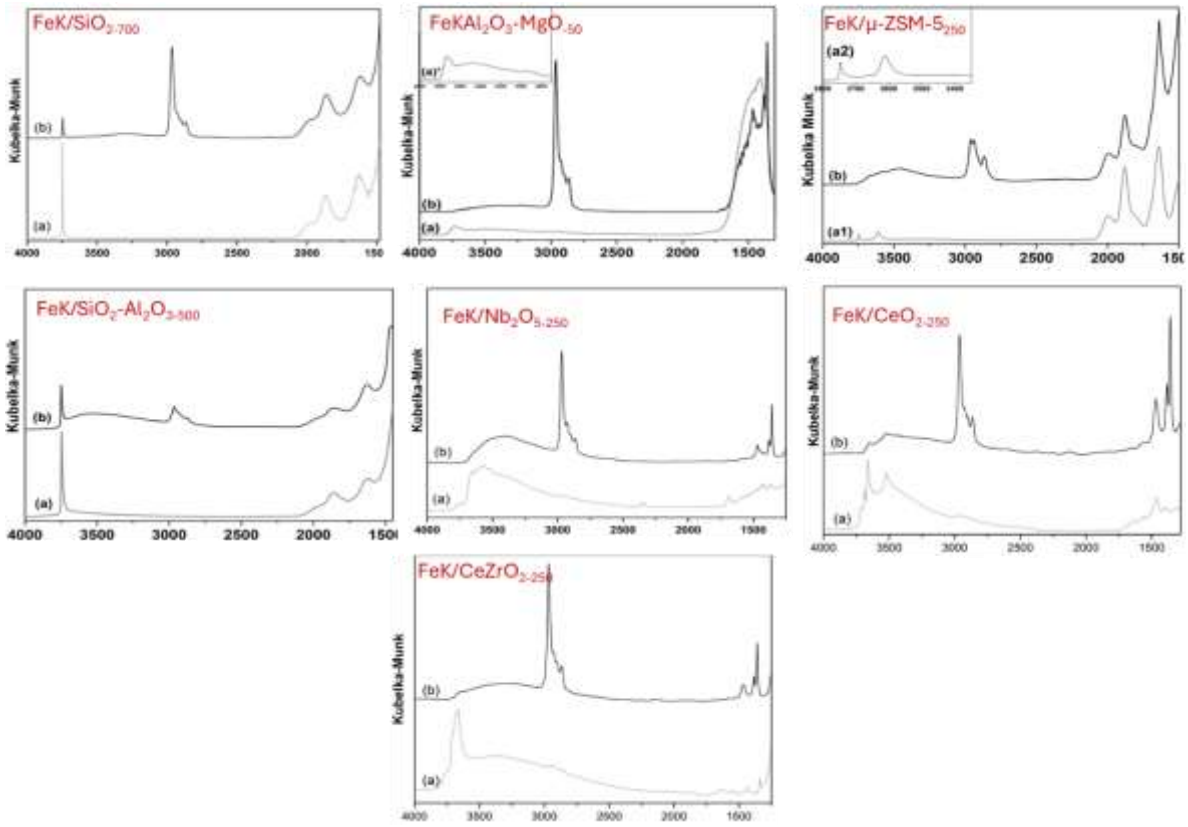

Fig. S8. DRIFT spectra of (a) dehydroxylated supports at different temperatures and (b) after surface modification with [{(THF)$_2$KFe(O*t*Bu)$_3$}$_2$] complex.

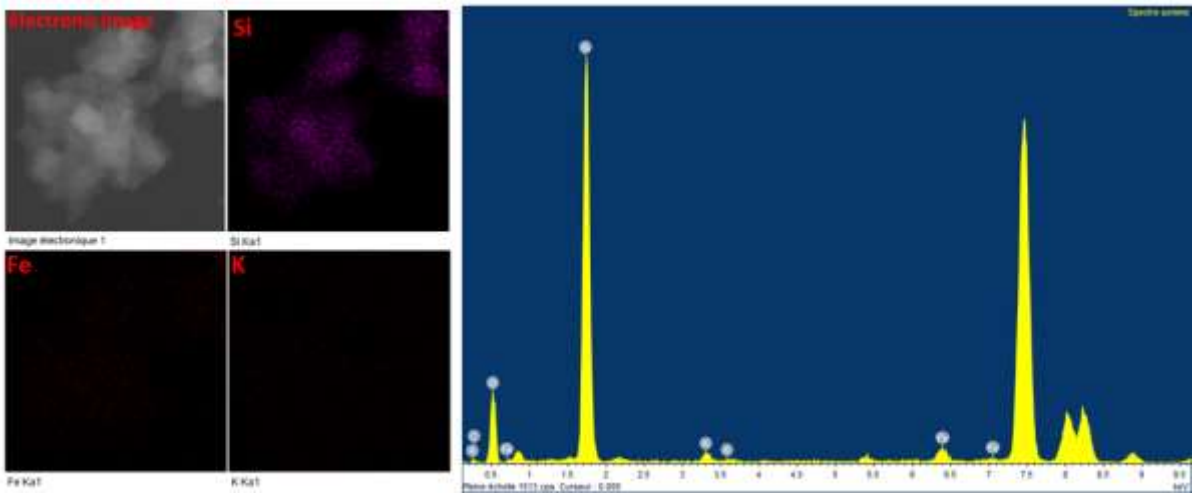

Fig. S9. EDX mapping (left) and EDX spectrum (right) of **FeK/SiO$_{2\text{-}700}$**.

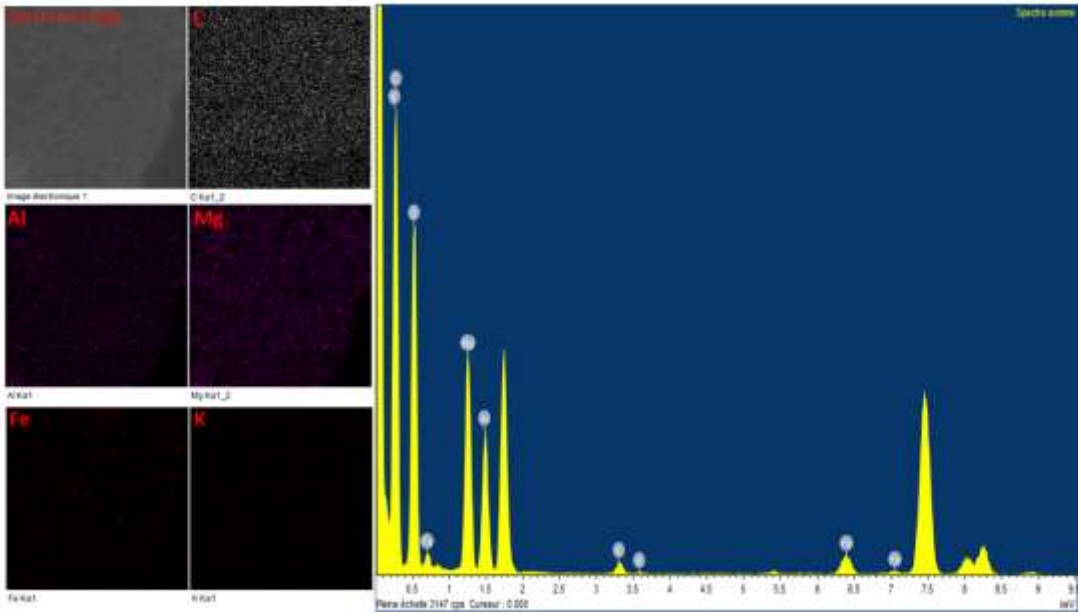

Fig. S10. EDX mapping (left) EDX spectrum (right) of **FeK/Al_2O_3-MgO$_{-500}$.**

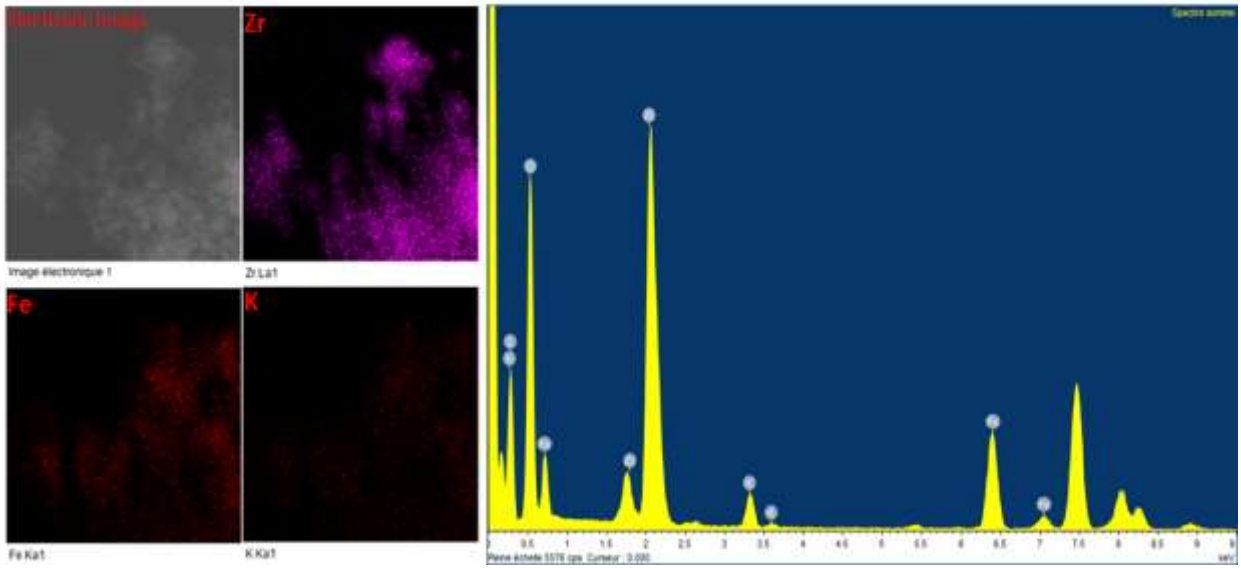

Fig. S11. EDX mapping (left) EDX spectrum (right) of **FeK/$ZrO_2$$_{-250}$.**

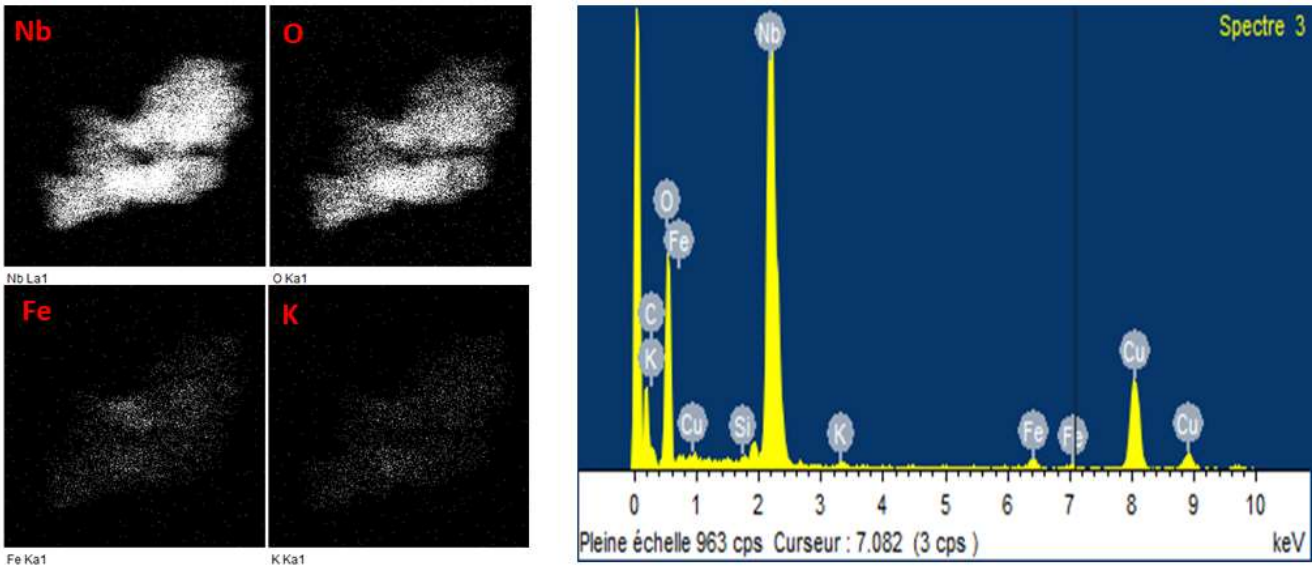

Fig. S12. EDX mapping (left) EDX spectrum (right) of **FeK/Nb$_2$O$_{5\text{-}250}$**.

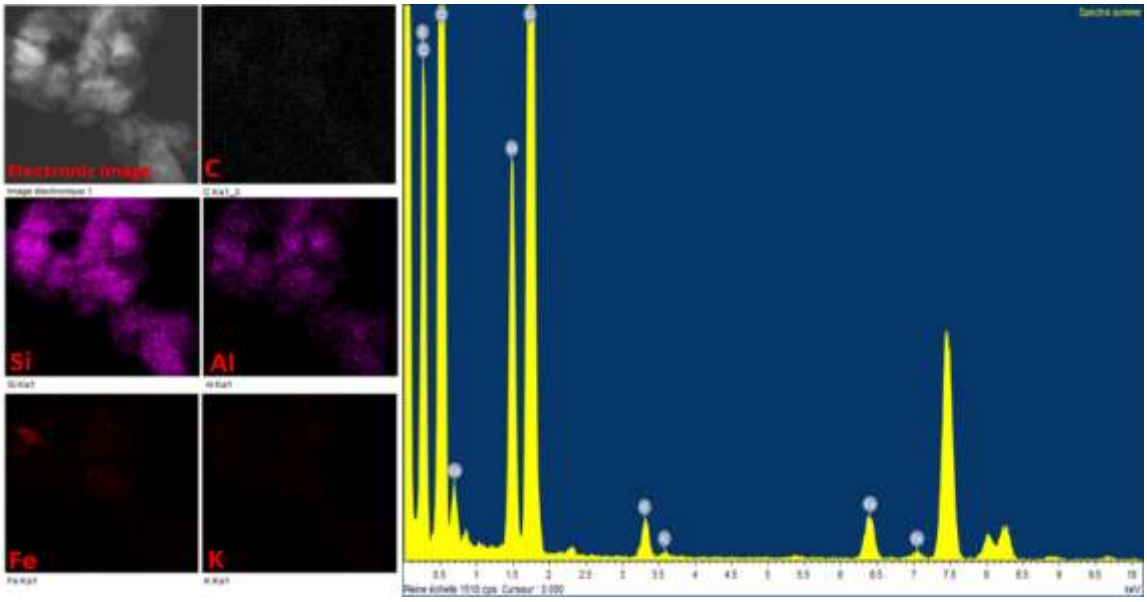

Fig. S13. EDX mapping (left) and EDX spectrum (right) of **FeK/SiO$_2$-Al$_2$O$_{3\text{-}500}$**.

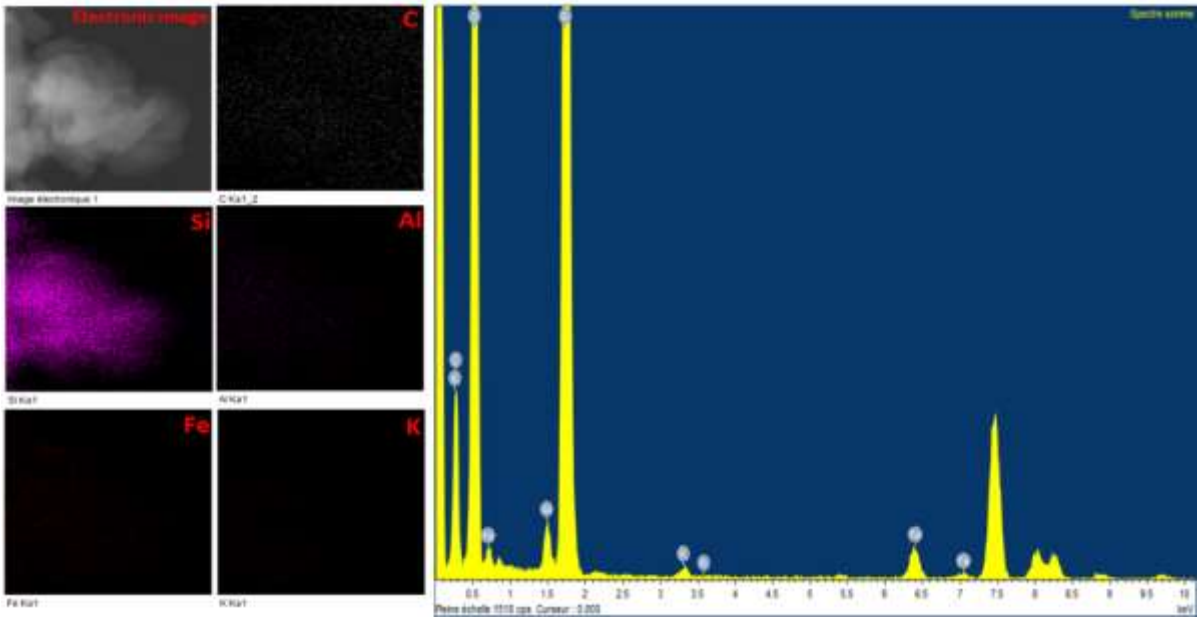

Fig. S14. EDX mapping (left) and EDX spectrum (right) of **FeK/µ-ZSM-5**$_{\text{-250}}$.

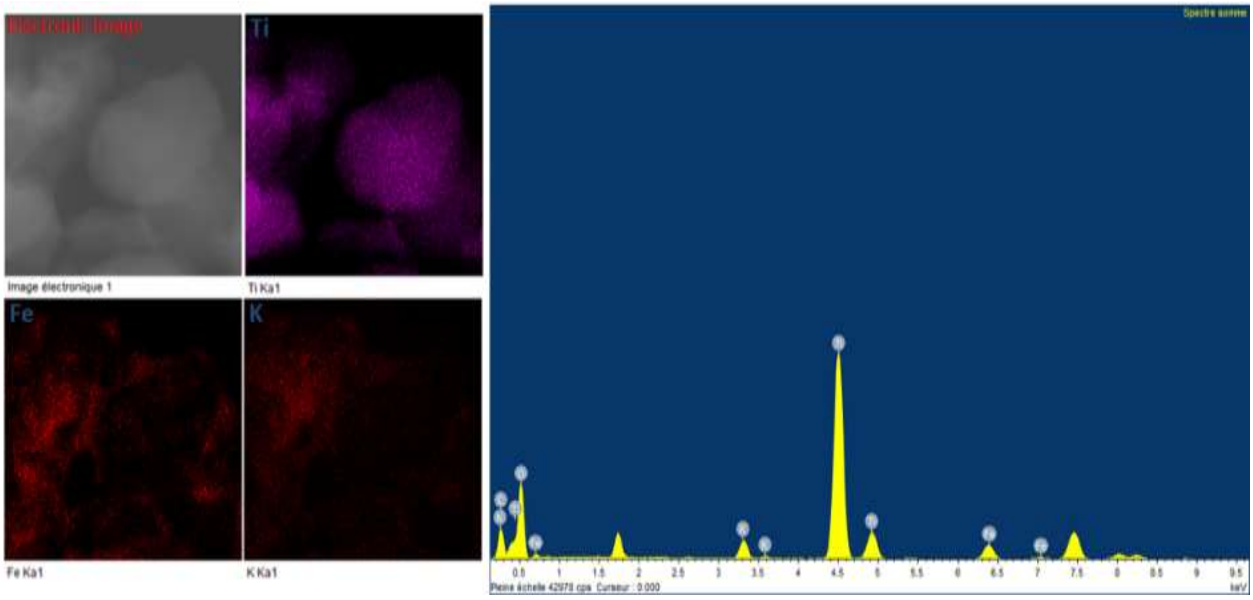

Fig. S15. EDX mapping (left) EDX spectrum (right) of **FeK/TiO**$_{\text{2-700}}$.

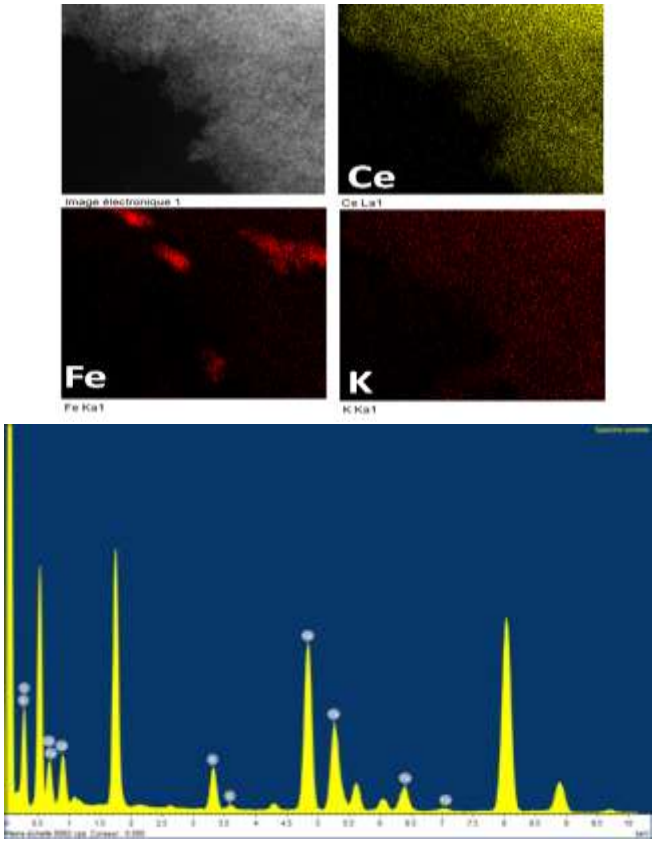

Fig. S16. EDX mapping and spectrum of **FeK/CeO$_{2\text{-}250}$** (1wt% Fe loading).

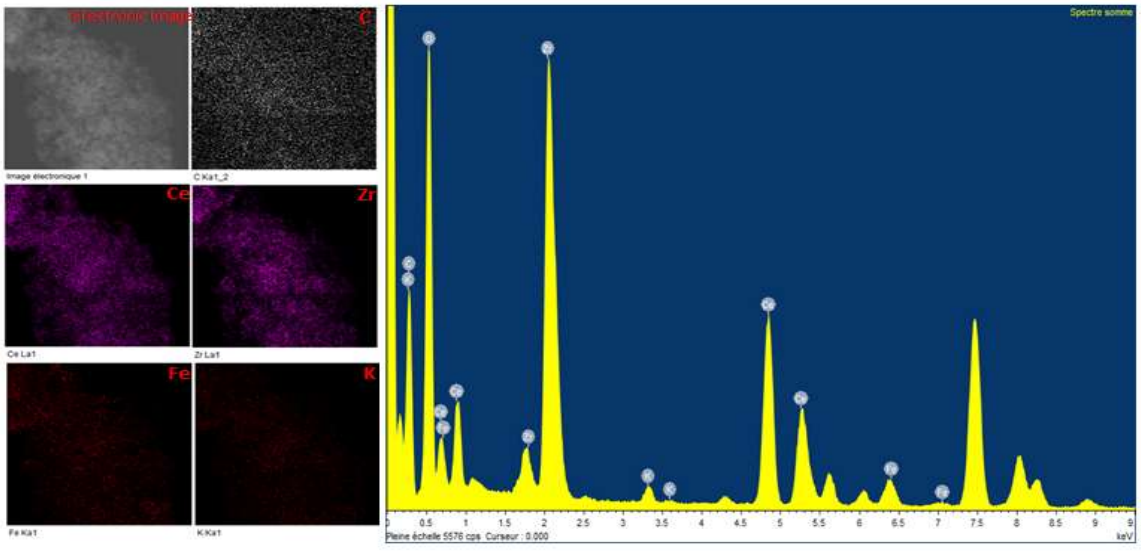

Fig. S17. EDX mapping (left) EDX spectrum (right) of **FeK/CeZrO$_{x\text{-}250}$**.

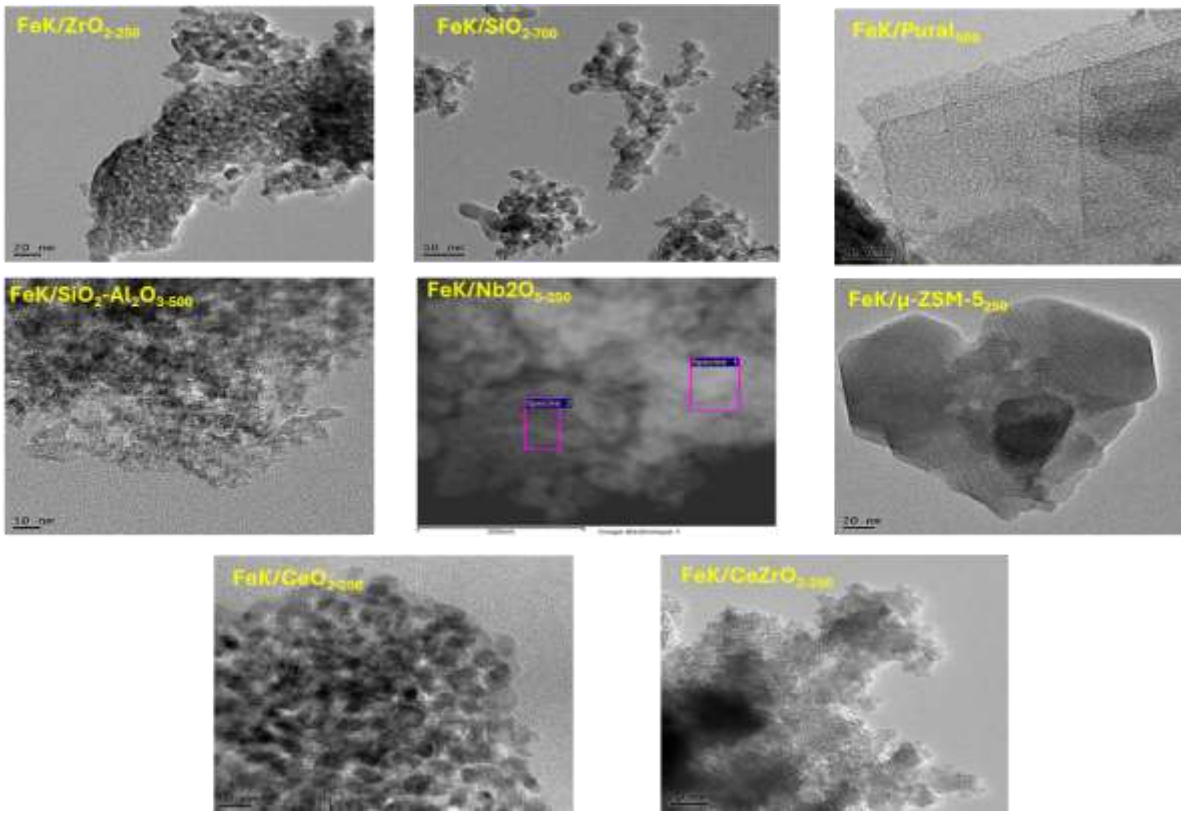

Fig. S18. HRTEM image of [{(THF)$_2$KFe(O*t*Bu)$_3$}$_2$] complex grafted on different nature of supports.

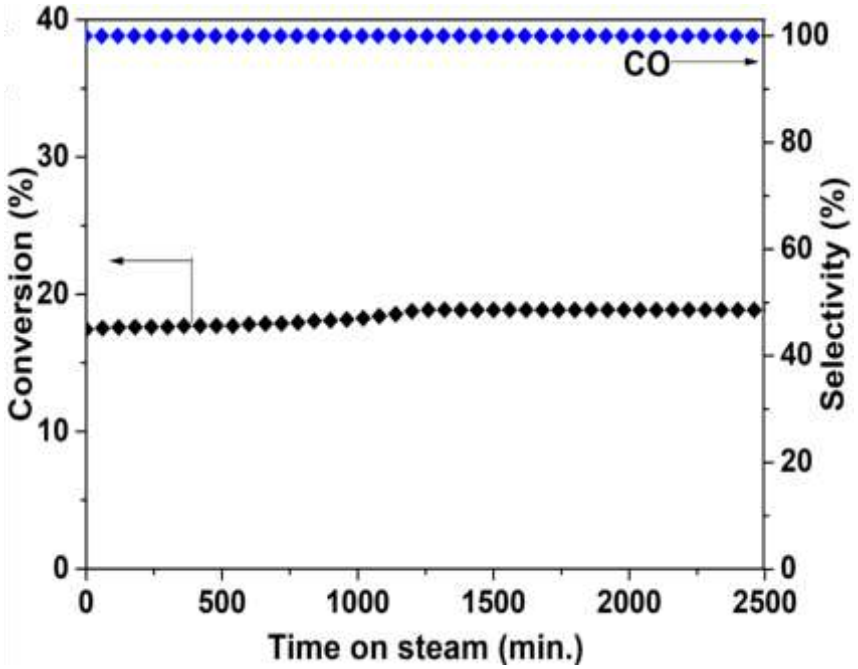

Fig. S19. CO_2 conversion (black) and CO selectivity (blue) over **FeK/SiO$_{2\text{-}700}$** (Feed composition: CO_2/H_2 :1/3, flow = 3 ml.min^{-1}, 400 °C, 30 bars).

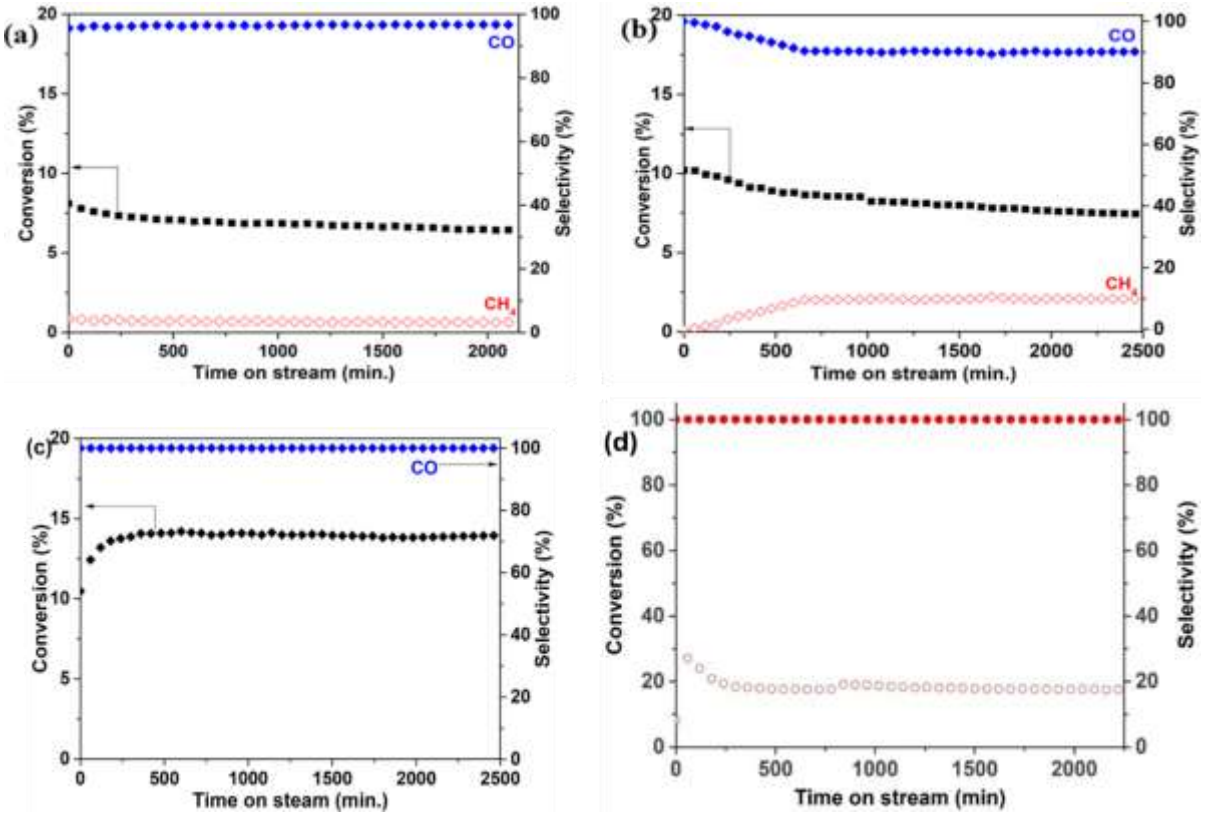

Fig. S20. CO_2 conversion and CO selectivity over (a) **FeK/SiO_2-Al_2O_3-500**, (b) **FeK/μ-H-ZSM-5-250**, (c) **FeK/Nb_2O_5-250** (d) **FeK/Al_2O_3-MgO-500** (Feed composition: CO_2/H_2 :1/3, flow = 3 ml.min^{-1}, 400 °C, 30 bars).

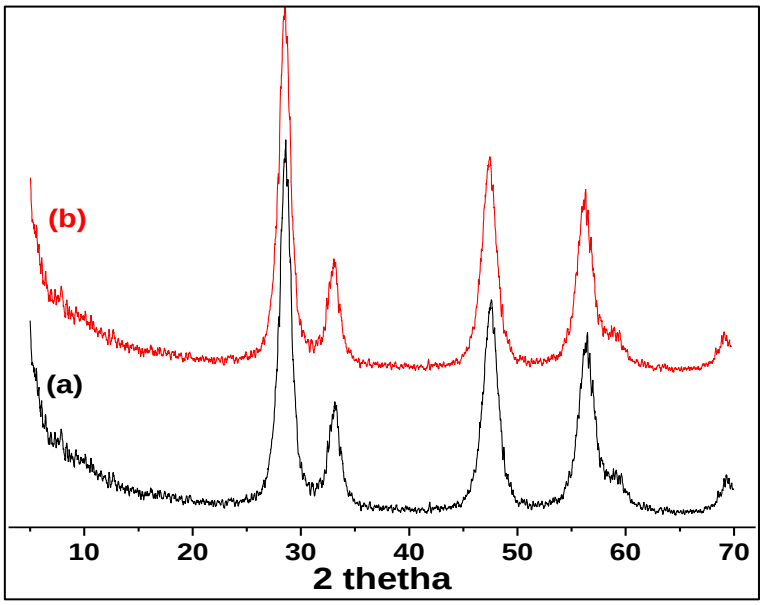

Fig. S21. X-ray diffraction pattern of **FeK/CeO_2-250** catalyst (a) before and (b) after catalytic test at 400 °C, 30 bar for ca. 40h.

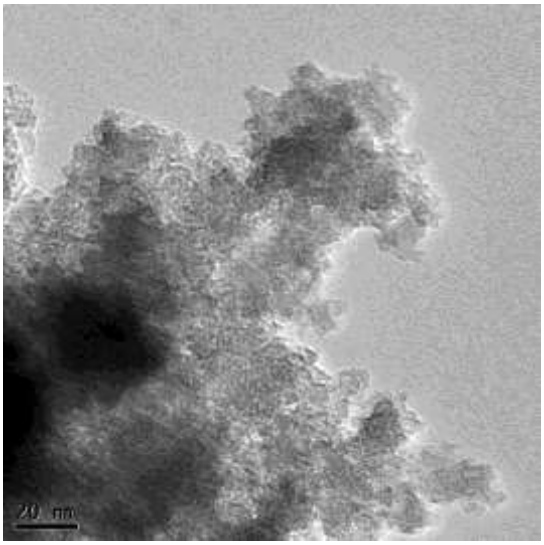

Fig. S22. HRTEM image of **FeK/CeO$_{2\text{-}250}$** catalyst (a) before and (b) after catalytic test at 400 °C, 30 bar for ca. 40h.

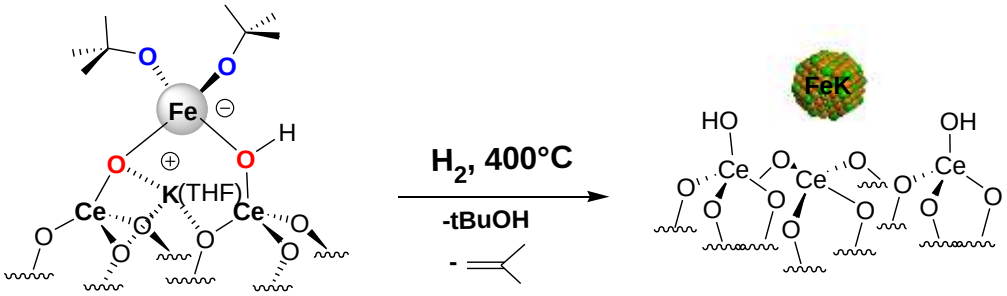

Scheme S1. Partial formation of FeK nanoparticle during CO_2 reduction over **FeK/CeO$_{2\text{-}250}$**.

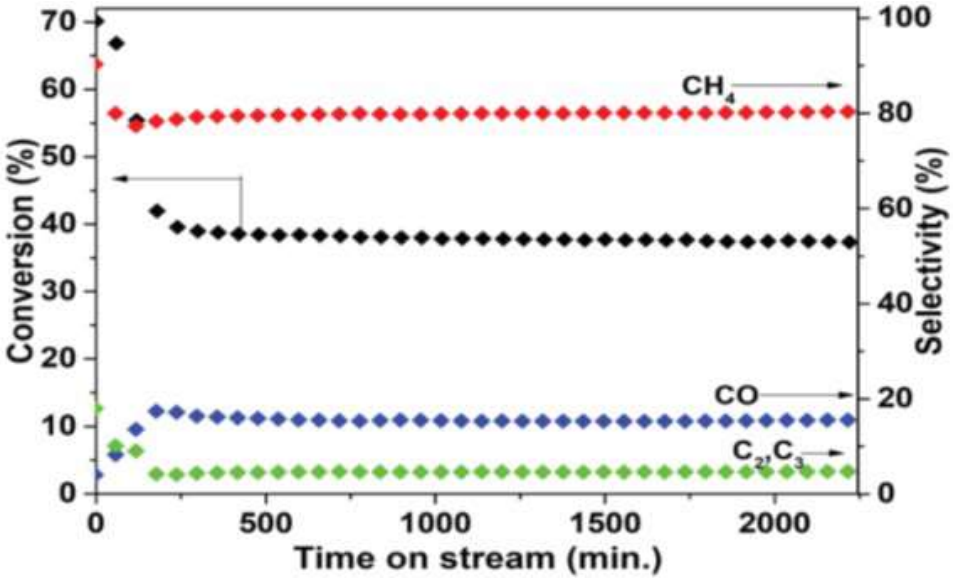

Fig. S23. CO_2 conversion and products selectivities over catalyst **FeK/CeO$_{2\text{-}250}$** reduced at 500°C (Feed composition: CO_2/H_2 :1/3, flow = 3 ml.min^{-1}, 400 °C, 30 bars).